The Astrophysical Journal Letters, 993:L6 (25pp), 2025 November 1 https://doi.org/10.3847/2041-8213/ae0b4d

The Most Luminous Known Fast Blue Optical Transient AT 2024wpp: Unprecedented Evolution and Properties in the X-Rays and Radio

Nayana A. J.[1,2], Raffaella Margutti[1,2,3], Eli Wiston[1,2], Tanmoy Laskar[4], Giulia Migliori[5], Ryan Chornock[1,2], Timothy J. Galvin[6], Natalie LeBaron[1,2], Aprajita Hajela[7], Collin T. Christy[8], Itai Sfaradi[1,2], Daichi Tsuna[9,10], Olivia Aspegren[1], Fabio De Colle[11], Brian D. Metzger[12,13], Wenbin Lu[1,2,14], Paz Beniamini[15], Daniel Kasen[2,16,17], Edo Berger[18], Brian W. Grefenstette[19], Kate D. Alexander[20], G. C. Anupama[21], Deanne L. Coppejans[22], Luigi F. Cruz[23], David R DeBoer[24,25], Maria R. Drout[26], Wael Farah[1,23,27], Xiaoshan Huang[28], W. V. Jacobson-Galán[29,40], Dan Milisavljevic[30,31], Alexander W. Pollak[23], Nathan J. Roth[32,33], Huei Sears[34], Andrew Siemion[23,27,35,36,37,38], Sofia Z. Sheikh[23,27], James F. Steiner[18], and Indrek Vurm[39]

[1] Department of Astronomy, University of California, Berkeley, CA 94720-3411, USA; nayana@berkeley.edu
[2] Berkeley Center for Multi-messenger Research on Astrophysical Transients and Outreach (Multi-RAPTOR), University of California, Berkeley, CA 94720-3411, USA
[3] Department of Physics, University of California, 366 Physics North MC 7300, Berkeley, CA 94720, USA
[4] Department of Physics & Astronomy, University of Utah, Salt Lake City, UT 84112, USA
[5] INAF Istituto di Radioastronomia, via Gobetti 101, 40129 Bologna, Italy
[6] ATNF, CSIRO Space & Astronomy, P.O. Box 1130, Bentley, WA 6102, Australia
[7] DARK, Niels Bohr Institute, University of Copenhagen, Jagtvej 155, 2200 Copenhagen, Denmark
[8] Department of Astronomy/Steward Observatory, 933 North Cherry Avenue, Room N204, Tucson, AZ 85721-0065, USA
[9] TAPIR, Mailcode 350-17, California Institute of Technology, Pasadena, CA 91125, USA
[10] Research Center for the Early Universe (RESCEU), School of Science, The University of Tokyo, 7-3-1 Hongo, Bunkyo-ku, Tokyo 113-0033, Japan
[11] Instituto de Ciencias Nucleares, Universidad Nacional Autónoma de México, Apartado Postal 70-264, 04510 México, CDMX, Mexico
[12] Department of Physics and Columbia Astrophysics Laboratory, Columbia University, New York, NY 10027, USA
[13] Center for Computational Astrophysics, Flatiron Institute, 162 5th Avenue, New York, NY 10010, USA
[14] Theoretical Astrophysics Center, University of California, Berkeley, CA 94720-3411, USA
[15] Department of Natural Sciences, The Open University of Israel, P.O Box 808, Ra'anana 4353701, Israel
[16] Department of Physics and Astronomy, University of California, Berkeley, CA 94720, USA
[17] Nuclear Science Division, Lawrence Berkeley National Laboratory, 1 Cyclotron Road, Berkeley, CA 94720, USA
[18] Center for Astrophysics | Harvard & Smithsonian, 60 Garden Street, Cambridge, MA 02138-1516, USA
[19] Space Radiation Laboratory, California Institute of Technology, 1200 E. California Boulevard, Pasadena, CA 91125, USA
[20] Department of Astronomy/Steward Observatory, 933 North Cherry Avenue, Rm. N204, Tucson, AZ 85721-0065, USA
[21] Indian Institute of Astrophysics, II Block, Koramangala, Bangalore 560034, India
[22] Department of Physics, University of Warwick, Coventry CV 4 7AL, UK
[23] SETI Institute, 339 Bernardo Avenue, Suite 200, Mountain View, CA 94043, USA
[24] Radio Astronomy Laboratory, University of California, Berkeley, CA, 94720, USA
[25] Sub-department of Astrophysics, University of Oxford, Oxford, OX1-3RH, UK
[26] David A. Dunlap Department of Astronomy & Astrophysics, University of Toronto, 50 St George Street, Toronto, ON M5S 3H4, Canada
[27] Berkeley SETI Research Centre, University of California, Berkeley, CA 94720, USA
[28] California Institute of Technology, TAPIR, Mail Code 350-17, Pasadena, CA 91125, USA
[29] Department of Astronomy and Astrophysics, California Institute of Technology, Pasadena, CA 91125, USA
[30] Purdue University, Department of Physics and Astronomy, 525 Northwestern Avenue, West Lafayette, IN 47907, USA
[31] Integrative Data Science Initiative, Purdue University, West Lafayette, IN 47907, USA
[32] Lawrence Livermore National Laboratory, P.O. Box 808, Livermore, CA 94550, USA
[33] Department of Physics, American University, 4400 Massachusetts Avenue NW, Washington, DC 20016, USA
[34] Department of Physics and Astronomy, Rutgers, The State University of New Jersey, 136 Frelinghuysen Road, Piscataway, NJ 08854-8019, USA
[35] Astrophysics, Department of Physics, University of Oxford, Keble Road, Oxford, OX1 3RH, UK
[36] Breakthrough Listen, Astrophysics, Department of Physics, The University of Oxford, Keble Road, Oxford OX1 3RH, UK
[37] Department of Physics and Astronomy, University of Manchester, UK
[38] University of Malta, Institute of Space Sciences and Astronomy, Msida, MSD2080, Malta
[39] Tartu Observatory, University of Tartu, Tõravere, 61602 Tartumaa, Estonia

Received 2025 August 29; revised 2025 September 17; accepted 2025 September 20; published 2025 October 24

Abstract

We present X-ray (0.3–79 keV) and radio (0.25–203 GHz) observations of the most luminous fast blue optical transient (LFBOT) AT 2024wpp at $z = 0.0868$, spanning 2–280 days after first light. AT 2024wpp shows luminous ($L_X \approx 1.5 \times 10^{43}$ erg s^{-1}), variable X-ray emission with a Compton hump peaking at $\delta t \approx 50$ days. The X-ray spectrum evolves from a soft ($F_\nu \propto \nu^{-0.6}$) to an extremely hard state ($F_\nu \propto \nu^{1.26}$) accompanied by a rebrightening at $\delta t \approx 50$ days. The X-ray emission properties favor an embedded high-energy source shining through asymmetric expanding ejecta. We detect radio emission peaking at $L_{9\,\mathrm{GHz}} \approx 1.7 \times 10^{29}$ erg s^{-1} Hz^{-1} at

---

[40] NASA Hubble Fellow.

$\delta t \approx 73$ days. The spectral evolution is unprecedented: the early millimeter fluxes rise nearly an order of magnitude during $\delta t \approx 17$–32 days, followed by a decline in spectral peak fluxes. We model the radio emission as synchrotron radiation from an expanding blast wave interacting with a dense environment ($\dot{M} \sim 10^{-3}\,M_\odot\,\mathrm{yr}^{-1}$ for $v_w = 1000\,\mathrm{km\,s^{-1}}$). The inferred outflow velocities increase from $\Gamma\beta c \approx 0.07c$ to $0.42c$ during $\delta t \approx 32$–73 days, indicating an accelerating blast wave. We interpret these observations as a shock propagating through a dense shell of radius $\approx 10^{16}$ cm and then accelerating into a steep density profile $\rho_{\rm CSM}(r) \propto r^{-3.1}$. All radio-bright LFBOTs exhibit similar circumstellar medium (CSM) density profiles ($\rho_{\rm CSM} \propto r^{-3}$), suggesting similar progenitor processes. The X-ray and radio properties favor a progenitor involving super-Eddington accretion onto a compact object launching mildly relativistic disk wind outflows.

Unified Astronomy Thesaurus concepts: Transient sources (1851); Time domain astronomy (2109); High energy astrophysics (739)

1. Introduction

High-cadence, wide-field optical transient surveys have been populating the phase space of transients with a variety of new fast-timescale events. A noteworthy class is fast blue optical transients (FBOTs), characterized by rapid rise to peak brightness ($\lesssim$10 days), persistent blue colors, and peak optical luminosities reaching $L_{\rm pk} \gtrsim 10^{45}\,\mathrm{erg\,s^{-1}}$. These properties are difficult to reconcile in traditional supernova (SN) models (M. R. Drout et al. 2014; I. Arcavi et al. 2016; M. Tanaka et al. 2016; M. Pursiainen et al. 2018; A. Rest et al. 2018). FBOTs are intrinsically rare, with a rate between 1% and 10% of the core-collapse SN (CCSN) rate in the local Universe (W. Li et al. 2011; M. R. Drout et al. 2014; M. Pursiainen et al. 2018; Y. Tampo et al. 2020). Luminous FBOTs (LFBOTs), a subclass of FBOTs with $L_{\rm pk} > 10^{43}\,\mathrm{erg\,s^{-1}}$, show bright X-ray and radio emission. LFBOTs are even rarer, with an intrinsic rate of only $\lesssim$0.1% of that of CCSNe (D. L. Coppejans et al. 2020; A. Y. Q. Ho et al. 2020, 2023c).

While tens of LFBOTs have been detected in optical surveys, only a small fraction have been followed up in X-ray and radio bands. To date, there are only seven LFBOTs with detailed X-ray and radio observations: the prototypical LFBOT AT 2018cow (A. Y. Q. Ho et al. 2019; R. Margutti et al. 2019), AT 2018lug (A. Y. Q. Ho et al. 2020), the first LFBOT with X-ray and radio detection CSS 161010 (D. L. Coppejans et al. 2020), AT 2020xnd (J. S. Bright et al. 2022; A. Y. Q. Ho et al. 2022), AT 2020mrf (Y. Yao et al. 2022), AT 2022tsd (A. Y. Q. Ho et al. 2023b; D. Matthews et al. 2023), and AT 2023fhn (A. A. Chrimes et al. 2024a, 2024b). These studies resulted in various critical insights into the nature of LFBOTs. Luminous and variable X-ray emission from AT 2018cow was interpreted as evidence for a central engine powering the transient (R. Margutti et al. 2019). AT 2020mrf (Y. Yao et al. 2022) and AT 2022tsd (A. Y. Q. Ho et al. 2023b) showed extremely luminous X-ray emission, exceeding that of AT 2018cow by an order of magnitude and comparable to that of cosmological gamma-ray bursts (GRBs). Meanwhile, radio observations have revealed a range of outflow velocities: mildly relativistic in the case of CSS 161010 (D. L. Coppejans et al. 2020), AT 2020lug (A. Y. Q. Ho et al. 2020), and AT 2023fhn (A. A. Chrimes et al. 2024a), and nonrelativistic in the cases of AT 2018cow (A. Y. Q. Ho et al. 2019; R. Margutti et al. 2019), AT 2020mrf (Y. Yao et al. 2022), AT 2020xnd (J. S. Bright et al. 2022; A. Y. Q. Ho et al. 2022), and AT 2022tsd (A. Y. Q. Ho et al. 2023b). Although these studies on individual events have significantly advanced our understanding of FBOTs, the overall sample remains small. Hence, it is still unclear whether the presence of a central engine, the origin of high-energy emission, and the observed range in outflow velocities are generic features of FBOTs or reflect heterogeneity in the population. This highlights the need for detailed X-ray and radio observations of additional FBOTs.

AT 2024wpp is the newest addition to the class of LFBOTs with detailed multiwavelength observations. It was discovered on 2024 September 25.44 UT (MJD 60578.4) in the ZTF survey data (A. Y. Q. Ho et al. 2024) at a redshift of $z = 0.0868$ (D. A. Perley et al. 2024). The transient brightened by $\approx$3 mag in a day with blue colors $g - r = -0.4$ mag. X-ray emission was detected in the subsequent Swift (G. Srinivasaragavan et al. 2024) and the Nuclear Spectroscopic Telescope Array (NuSTAR; R. Margutti et al. 2024) follow-up observations. Radio emission was detected in the Very Large Array (VLA) X-band (10 GHz) and Ku-band (15 GHz) observations with a spectral luminosity of $L_{10\,\rm GHz} \approx 5 \times 10^{28}\,\mathrm{erg\,s^{-1}\,Hz^{-1}}$ at $\approx$29 days post-discovery (G. Schroeder et al. 2024). E. O. Ofek et al. (2025) reported nondetection of any minute-timescale optical flares in AT 2024wpp with a 2σ upper limit of $<$0.02 on the flare's duty cycle. Our detailed UV−optical−near-IR (NIR) campaign of AT 2024wpp in the first 100 days is presented in our companion paper (LeBaron et al. 2025, hereafter Paper I), and we summarize the main observational findings below. AT 2024wpp is the most luminous FBOT to date, with peak luminosity $L_{\rm pk} \approx (2$–$4) \times 10^{45}$ erg (in agreement with M. Pursiainen et al. 2025) and a detailed UV light curve that samples the pre-peak phase of an FBOT for the first time. The UV−optical spectrum remains featureless and dominated by blue thermal continuum emission for weeks. The blackbody temperature at optical peak is $T > 30{,}000$ K and remains at $T \gtrsim 20{,}000$ K for weeks. At $\delta t \approx 35$ days, faint H and He spectral features are detected with some similarities to the phenomenology of AT 2018cow (R. Margutti et al. 2019; D. A. Perley et al. 2019). Finally, we find evidence for an NIR excess of emission, which might be related to preexisting dust or free–free emission in a high-density medium. Despite being at a distance of 411 Mpc, the exceptional luminosity of AT 2024wpp allowed us to carry out unprecedented multiwavelength follow-up observations in the optical, UV, NIR, X-ray, and radio bands. This extensive data set of AT 2024wpp is superior to even the prototypical FBOT AT 2018cow and provides us the unique opportunity to study this transient in exquisite detail.

In this Letter, we present extensive X-ray (soft to hard) and radio (sub-GHz to millimeter-band) follow-up observations of AT 2024wpp spanning $\delta t \approx 2$–280 days after first light. We refer to Paper I where applicable to place our results in a broader context and build a comprehensive physical picture.

The Letter is structured as follows: We present the X-ray and radio observations in Sections 2 and 3, respectively. Section 4 presents inferences based on X-ray observations. The properties of the shock wave and the environment are presented in Sections 5 and 6 based on radio observations. We discuss the properties of AT 2024wpp in the context of other LFBOTs in Section 7. Plausible physical scenarios are discussed in Section 8, and conclusions are drawn in Section 9. We adopt the cosmological parameters of Lambda cold dark matter (ΛCDM) $H_0 = 67.4\,\mathrm{km\,s^{-1}\,Mpc^{-1}}$, $\Omega_m = 0.315$, $\Omega_\Lambda = 0.685$ (Planck Collaboration et al. 2020). For these parameters, the redshift $z = 0.0868$ of AT 2024wpp (D. A. Perley et al. 2024) corresponds to a luminosity distance of 411 Mpc. Following Paper I, we adopt MJD 60578.3 as our reference time $t = 0$ days. Times are in the observer frame unless noted otherwise.

2. Broadband X-Ray Observations

2.1. Swift-XRT (0.3–10 keV)

Prompt observations of AT 2024wpp with the X-Ray Telescope (XRT; D. N. Burrows et al. 2005) on board the Neil Gehrels Swift observatory (N. Gehrels et al. 2004) were obtained starting on 2024 September 27, 09:45:24 UT ($\delta t = 2.1$ days; PI: Coughlin; exposure time of ≈2.2 ks; target ID 16843). We triggered an intense campaign under our Swift Guest Observer program (PI: Margutti; total of 116 ks; target IDs: 16848, 18973) covering the time interval $\delta t = 4.7$–118.7 days. We processed the XRT data with HEASoft v6.34 and corresponding calibration files. We extracted a 0.3–10 keV count-rate light curve and rebinned to have a minimum number of 5 counts per bin following standard procedures (P. A. Evans et al. 2009; R. Margutti et al. 2013).

We extracted several XRT spectra at salient phases of the FBOT X-ray light curve (e.g., initial “plateau” at $\delta t = 2.1$–6.6 days, decay phase at $\delta t = 6.7$–34.5 days, late-time “flare” at $\delta t = 39$–59 days, and post-flare phase at $\delta t > 60$ days; see Figure 1) and around the time of acquisition of NuSTAR observations. We employed W-statistics to fit the spectra; we set the metal abundances to solar values with `aspl`, and we adopted the `tbabs` cross sections within `Xspec`. In all cases, the spectra are well modeled with an absorbed power-law model. We find no statistical evidence for intrinsic absorption in any individual spectrum or in joint spectral analysis once the fit solutions are verified with the `steppar` command: a neutral absorption column $\mathrm{NH_{int}} = 0\,\mathrm{cm^{-2}}$ is a statistically acceptable solution in all cases. We thus proceed with $\mathrm{NH_{int}} = 0\,\mathrm{cm^{-2}}$ in our following spectral fits and correct for the neutral hydrogen absorption component from the Galaxy only, which is $\mathrm{NH_{MW}} = 2.6 \times 10^{20}\,\mathrm{cm^{-2}}$ (HI4PI Collaboration et al. 2016).

We find clear evidence for spectral hardening of the source with time that becomes extreme at the time of the flare, followed by softening of the emission. These findings are confirmed and strengthened by our deep CXO, XMM-Newton (XMM), and coordinated NuSTAR observations. We end by noting (i) the presence of the well-known spurious correlation between the inferred $\mathrm{NH_{int}}$ and photon index that is due to the degeneracy between these two parameters in soft-X-ray only fits. This degeneracy is lifted by modeling broadband observations that span the soft and hard X-ray spectral range of Section 4. (ii) We also note that, with the exception of the flare peak time interval, the spectral fits that model the XRT data only tend to return softer photon indices than those from XRT +NuSTAR data (Table 1).

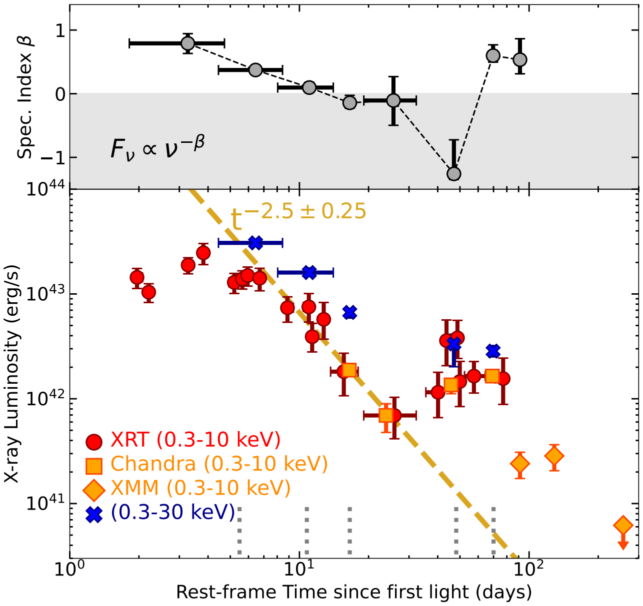

Figure 1. Top panel: evolution of the spectral photon index β with time (where $F_\nu \propto \nu^{-\beta}$), showing clear evidence for spectral hardening until the time of the flare peak at $\gtrsim$50 days, followed by softening of the emission. Aside from the flare peak, the plotted β values apply to the broadband soft +hard X-ray spectral range; at the time of the flare peak, when there is evidence for a BPL spectrum, the plotted value represents the index below the spectral break. The gray shaded area marks the region of the parameter space associated with a *rising* F_ν spectrum. Bottom panel: 0.3–10 keV unabsorbed luminosity light curve (red filled circles, orange squares, and orange diamonds for XRT, CXO, and XMM observations, respectively) and 0.3–30 keV light curve (blue crosses) derived from a self-consistent time-dependent flux calibration. Vertical gray dotted lines mark the time of broadband X-ray spectrum acquisition. Dashed gold line: best-fitting power-law luminosity decay in the time period 10–50 days.

2.2. Chandra X-Ray Observatory (0.3–10 keV)

We obtained four epochs of Chandra X-Ray Observatory (CXO) ACIS-S observations of AT 2024wpp under two Director’s Discretionary Time (DDT) programs (25509013 and 25509020; PI: Margutti). Acquired in the time period $\delta t = 17.8$–75.4 days, the CXO observations provide key information during the late decay, flare, and post-flare phases (Table 8). The CXO ACIS-S data have been reduced following standard practice with `CIAO v4.16` and corresponding calibration files. A bright X-ray source is detected with high confidence at the location of AT 2024wpp with `wavdetect`. For each epoch, we extracted a spectrum with `specextract` using a source region with radius of 2″ and a source-free background region with radius >35″. CXO observations are not sensitive to the $\mathrm{NH_{int}}$ parameter because of the limited effective area below ≈1 keV. We modeled the spectra with an absorbed power-law model as in Section 2.1. Remarkably, CXO observations acquired at the time of the flare peak at $\delta t \approx 50$ days indicate a rising $F_\nu \propto \nu^{1.26}$ spectrum. Spectral modeling is described in Section 4.

2.3. XMM-Newton (0.2–12 keV)

We acquired a sequence of three late-time, deep XMM observations of AT 2024wpp at $\delta t = 98.9$–99.5 days,

Table 1
X-Ray Spectral Parameters and Inferred Fluxes

δt[a] (days)	Model	Γ_1	Γ_2	$E_{\rm break}$[b] (keV)	$F_{\rm x}$[d] (10^{-13} cgs) [0.3–10 keV]	$F_{\rm x}$[d] (10^{-13} cgs) [0.3–30 keV]	$F_{\rm x}$[c,d] (10^{-13} cgs) [20–200 keV]	Instrument
2.1–5.0	SPL	$1.79^{+0.15}_{-0.16}$	⋯	⋯	$7.9^{+1.0}_{-1.0}$	$11.8^{+3.0}_{-2.0}$	$10.8^{+9.2}_{-5.5}$	XRT
5.0–9.0	SPL	$1.37^{+0.06}_{-0.04}$	⋯	⋯	$7.2^{+0.5}_{-0.3}$	$15.2^{+0.5}_{-0.5}$	$40.5^{4.3+}_{-6.4}$	XRT+NuSTAR
9.0–15.0	SPL	$1.10^{+0.08}_{-0.06}$	⋯	⋯	$2.9^{+0.2}_{-0.2}$	$7.9^{+0.5}_{-0.4}$	$39.1^{+6.9}_{-8.2}$	XRT+NuSTAR
17.4–18.6	SPL	$0.86^{+0.11}_{-0.08}$	⋯	⋯	$0.93^{+0.08}_{-0.07}$	$3.3^{+0.3}_{-0.4}$	$26.9^{+8.3}_{-8.1}$	CXO+NuSTAR
21.3–34.5	SPL	$0.89^{+0.37}_{-0.39}$	⋯	⋯	$0.34^{+0.01}_{-0.01}$	$1.2^{+0.7}_{-0.6}$	$8.9^{+13.5}_{-7.4}$	CXO+XRT
49.5–52.8	BPL	$-0.26^{+0.53}_{-0.09}$	$1.98^{+4.57}_{-0.42}$	$7.8^{+3.49}_{-0.33}$	$0.67^{+0.01}_{-0.01}$	$1.7^{+0.4}_{-0.7}$	$2.1^{+1.9}_{-2.0}$	CXO+NuSTAR
75.0–76.6	SPL	$1.60^{+0.17}_{-0.10}$	⋯	⋯	$0.81^{+0.07}_{-0.05}$	$1.4^{+0.2}_{-0.2}$	$2.2^{+1.2}_{-0.9}$	CXO+NuSTAR
98.9–99.5	SPL	$1.53^{+0.33}_{-0.22}$	⋯	⋯	$0.12^{+0.03}_{-0.03}$	$0.22^{+0.13}_{-0.09}$	$0.39^{+0.65}_{-0.31}$	XMM
139.7–140.2	SPL	1.53	⋯	⋯	$0.14^{+0.04}_{-0.04}$	$0.30^{+0.07}_{-0.07}$	$0.47^{+0.13}_{-0.13}$	XMM

Notes. The SPL model is parameterized as $F_\nu \propto \nu^{-\beta_1}$, where $\beta_1 = \Gamma_1 - 1$ and Γ_1 is the photon index. The BPL model is $F_\nu \propto \nu^{-\beta_1}$ for $\nu < \nu_{\rm break}$ and $F_\nu \propto \nu^{-\beta_2}$ for $\nu > \nu_{\rm break}$, $\beta_2 = \Gamma_2 - 1$, and Γ_2 is the photon index above the spectral break.

[a] Observer frame, with respect to time of first light.

[b] $E_{\rm break} \equiv h\nu_{\rm break}$.

[c] Based on the extrapolation of the SPL or BPL spectral model at higher energies not sampled by observations (i.e., it assumes no additional spectral break).

[d] Fluxes are unabsorbed and in units of erg $\rm s^{-1} cm^{-2}$.

$\delta t = 139.7$–140.2 days, and $\delta t = 279.1$–279.7 days under a Guest Investigator program (No. 090332; PI: Margutti; Table 8). The data from the three European Photon Imaging Camera (EPIC)-pn, MOS1, and MOS2 have been reduced with the Scientific Analysis System (SAS) v.20.0.0 and corresponding calibration files (CALDB 3.13). We filtered out time intervals with enhanced background due to proton flaring, which led to a significant reduction of the exposure time in the second XMM observation, especially for the pn camera. To assess the significance of the detection, for each observation we ran the EPIC source detection tasks `emosaic_prep` and `emosaicproc` for all three cameras simultaneously over the full 0.3–12 keV (0.2–12 keV) energy band and in three standard subenergy bands (i.e., 0.3–1.0 keV for the pn and 0.2–1 keV for the MOS, 1.0–7.5 keV, 7.5–12.0 keV).

A source is significantly detected at the location of AT 2024wpp in the full band in the first two observations, with a resulting detection maximum likelihood of `DET_ML`=71 and 12 ($\gtrsim 3\sigma$, Gaussian equivalent) for the first and second observations, respectively. The total net counts in each observation from the combined detector images are 155 ± 18 and 81 ± 18, respectively (0.2–12 keV energy band). No source is detected in the third observation, and we infer a 3σ limit of <0.001 counts $\rm s^{-1}$ in the 0.3–10 keV band from the EPIC-pn exposure. For the first observation, we extracted three source spectra (i.e., one each for the EPIC-pn, MOS1, and MOS2) using a $30''$-radius region, and we estimated the background from a source-free region on the same chip. The limited statistics of the second observation do not allow spectral modeling, and we thus inferred the observed flux from the count rate, assuming a photon index $\Gamma = 1.6$, as the limited number statistics did not allow us to constrain the spectrum. The same model is assumed for the count-to-flux conversion of the upper limit of the third and fourth epochs.

2.4. NuSTAR (3–79 keV)

We acquired a total of five epochs of hard X-ray observations of AT 2024wpp with NuSTAR. The first three epochs were acquired starting on 2024 September 30, 19:21:09 UT ($\delta t = 6.0$ days) under a DDT program (PI: Margutti), with the remaining two observations acquired under a joint XMM–Newton–NuSTAR Guest Observer program (No. 090332; PI: Margutti). A complete log of NuSTAR observations is reported in Table 8.

We used `nupipeline` and `nuproducts` to extract spectra and response files using the NuSTAR Data Analysis Software (v2.1.2) and calibration files (ver. 20240104). The source extraction region has a radius of $50''$, and we estimated the local background with a nearby source-free region. We checked for the presence of solar flares and significant radiation belt backgrounds using standard background plots and custom `Python` scripts. When present, we removed the intervals of time affected by the enhanced background by redefining the good time intervals (GTIs) of extraction of our products. A source is blindly detected at the location of the transient until $\delta t \approx 20$ days, which represents the latest NuSTAR detection of an FBOT to date. AT 2024wpp is weakly detected at <10 keV in the NuSTAR A-module at $\approx$50 days, and it is not significantly detected at $\approx$75 days. These hard X-ray detections, weak detections, and nondetections are critical to anchor the broadband spectral fits of Section 4.

3. Broadband Radio Observations

3.1. ALMA

We observed AT 2024wpp with the Atacama Large Millimeter/submillimeter Array (ALMA) in Cycle 11 as part of DDT programs 2024.A.00003.T and 2024.A.00009.T (PI: Nayana). The observations were acquired on 2024 October 14 ($\delta t \approx 19$ days) and October 31 ($\delta t \approx 36$ days) in bands 3 (97.5 GHz) and 5 (203 GHz). ALMA was in its C3 configuration, with 45–48 working antennae providing baselines ranging from 14 to 499 m. J0334−4008 was used as the flux density and bandpass calibrator at both bands on the 2024 October 14 observations, and J0006−0623 was used on the 2024 October 31 observations. J0246−1236 and J0241−0815 were used as the phase calibrators in bands 3 and 5, respectively, at both epochs. The on-source integration time was $\approx$9 minutes in band 3 and $\approx$20 minutes in band 5. We downloaded the pipeline-generated images from the ALMA archive and estimated the flux density of the source using Common Astronomy Software Applications (CASA; CASA Team et al. 2022). The ALMA flux densities are reported in Table 3.

3.2. ATCA

The Australian Telescope Compact Array (ATCA) observed AT 2024wpp at seven epochs from 2024 October 10 ($\delta t \approx 15$ days) to 2025 March 19 ($\delta t \approx 175$ days) in the 15 mm, 7 mm, and 4 cm bands under the Non A-Priori Assignable (NAPA) project C3419 (PI: Nayana). At each frequency band, the data were recorded in two intermediate frequencies (IFs) each split into 2048 channels. PKS B1934−638 and PKS B0237−233 were used as the flux density and phase calibrators, respectively, in all three bands. The flux calibrator was also used to calibrate the bandpass in the 15 mm and 4 cm bands, whereas PKS B1921−293 was used as the bandpass calibrator in the 7 mm band. The total exposure was ≈3 hr in the 7 and 15 mm bands and 2.5 hr in the 4 cm band, resulting in ≈1.5−2 hr on source after overheads, respectively, for each band. The data were reduced using CASA following the standard flagging and calibration procedure, treating each IF and epoch separately. Calibrated data were imaged using two Taylor terms, adopting Briggs weighting. ATCA flux density measurements are presented in Table 4.

3.3. ATA

We observed the field of AT 2024wpp with the Allen Telescope Array (ATA; W. Farah et al. 2025, in preparation; A. W. Pollak et al. 2025, in preparation) on 2024 October 9 ($\delta t \approx 14$ days) and November 1 ($\delta t \approx 37$ days). The ATA is a radio interferometer that comprises 42 dishes, each with a diameter of 6.1 m, and can utilize up to four independent frequency tunings in the range of 1–10 GHz, each with ≈700 MHz bandwidth (J. S. Bright et al. 2023). Our observations were centered at 3 and 8 GHz. We used 3C 147 to calibrate the absolute flux scale and the bandpass response and J0241−082 to calibrate the time-dependent complex gains. We used a customized pipeline[41] utilizing CASA to reduce the data. Imaging was done using CASA task `TCLEAN` (A. R. Offringa & O. Smirnov 2017), adopting Briggs weighting. The source was not detected in our ATA observations (I. Sfaradi et al. 2024). We report 3σ image rms as flux density upper limits in Table 5.

3.4. MeerKAT

We observed AT 2024wpp with MeerKAT at three epochs: 2024 October 31 ($\delta t \approx 36$ days), November 15 ($\delta t \approx 51$ days), and December 11 ($\delta t \approx 77$ days) at L band under project code SCI-20230907-NA-01 (PI: Nayana). J0408−6545 was used as the flux density and bandpass calibrator, and J0240−2309 was used as the phase calibrator. The data were recorded using a correlator bandwidth of 856 MHz split into 4000 channels with an integration time of 8 s. We used the calibrated images produced by the SARAO Science Data Processor (SDP) pipeline.[42] The source was not detected in any of the MeerKAT images, and 3σ flux density limits are reported in Table 6.

3.5. GMRT

Giant Metrewave Radio Telescope (GMRT) observations of AT 2024wpp were acquired from 2024 October 10 to 2025 January 26 ($\delta t \approx 37$–123 days) in bands 3 (0.25–0.50 GHz), 4 (0.55–0.85 GHz), and 5 (1.00–1.46 GHz). We observed 3C 48 to calibrate the absolute flux densities and bandpass and J0240 −231 to calibrate the atmospheric phase fluctuations. The data were recorded using a correlator bandwidth of 200 MHz in bands 3 and 4 and 400 MHz in band 5, split into 2048 channels. The observations were done in standard continuum full polar mode with an integration time of 10 s. The GMRT data were reduced using Astronomical Image Processing Software (AIPS; E. W. Greisen 2003) following standard procedures. The data were initially inspected for nonworking antennas and radio-frequency-interference-prone channels and flagged using AIPS task UVFLAG. Single-channel calibration was done using a central channel, and the solutions were applied to the entire band. The fully calibrated target data were imaged using IMAGR. A few rounds of phase-only self-calibration were performed to improve the image quality. Radio emission associated with AT 2024wpp was not detected in any of the GMRT maps. We quote the details of GMRT observations and the 3σ flux density limit at the source position in Table 7.

4. X-Ray Modeling and Inferences

4.1. Joint Soft and Hard X-Ray Spectral Modeling and X-Ray Flux Calibration

We jointly fit the epochs with soft (Swift-XRT, XMM, or CXO) and hard (NuSTAR) X-ray data to constrain the broadband spectral properties of AT 2024wpp and their evolution. There is no evidence for thermal X-ray emission at any time, which is consistent with all the other FBOTs to date. We use an absorbed simple power-law (SPL) and a broken power-law (BPL) model within `Xspec`. We adopt solar abundances and `tbabs` cross sections with Galactic neutral hydrogen column density $\mathrm{NH_{MW}} = 2.6 \times 10^{20}\ \mathrm{cm}^{-2}$ (HI4PI Collaboration et al. 2016). For each epoch and source spectral model, we take two approaches to properly account for the low number statistics of source counts in NuSTAR.[43] In the first method, we perform full background and source spectral modeling adopting Cash statistics (W. Cash 1979) after ensuring that each bin in each spectrum contains at least one count. The source and background files are simultaneously fit with a background model for the background spectrum and a combination of source plus background model for the source file, with the background model parameters tied to the same values. This is the ideal approach to avoid statistically biased parameter inference, but it assumes that it is possible to approximate the background with an analytical function. As a second approach, we use the W-statistics after having ensured that every bin in the background spectrum contains enough counts. We find that the two methods lead to statistically consistent results; in the following, we report and show the results from the W-stat approach.

---

[41] https://github.com/joesbright/ATARI/

[42] https://skaafrica.atlassian.net/wiki/spaces/ESDKB/pages/338723406/

[43] See, e.g., https://giacomov.github.io/Bias-in-profile-poisson-likelihood/.

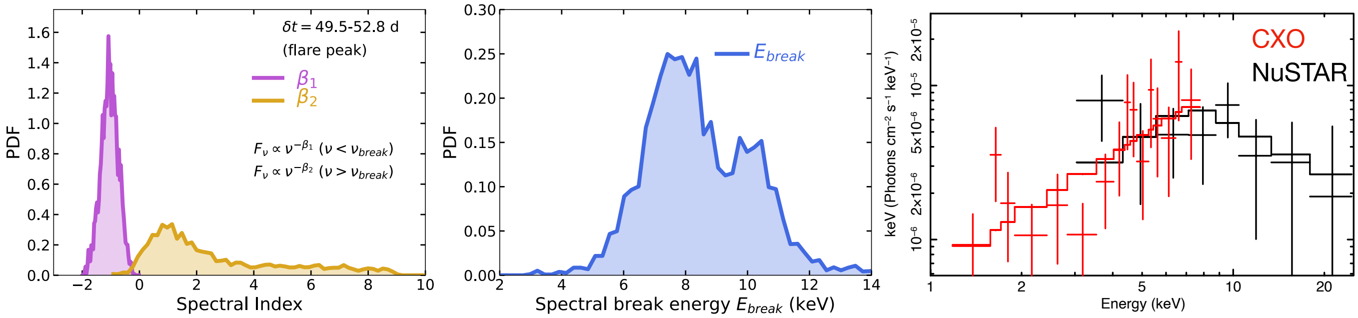

Figure 2. Probability density distributions of the spectral photon indices (left panel) and spectral break energy (middle panel), for the BPL model that best fits the broadband X-ray SED at the time of the flare peak (right panel, unfolded spectrum). The CXO data (red) indicate a rising spectrum with extreme properties: $F_\nu \propto \nu^{1.25}$. The lack of bright hard X-ray emission at the same time, as constrained by NuSTAR, demands the presence of a spectral break and significantly softer emission above $E_{\rm break}$, with the spectrum bending to $F_\nu \propto \nu^{-1}$.

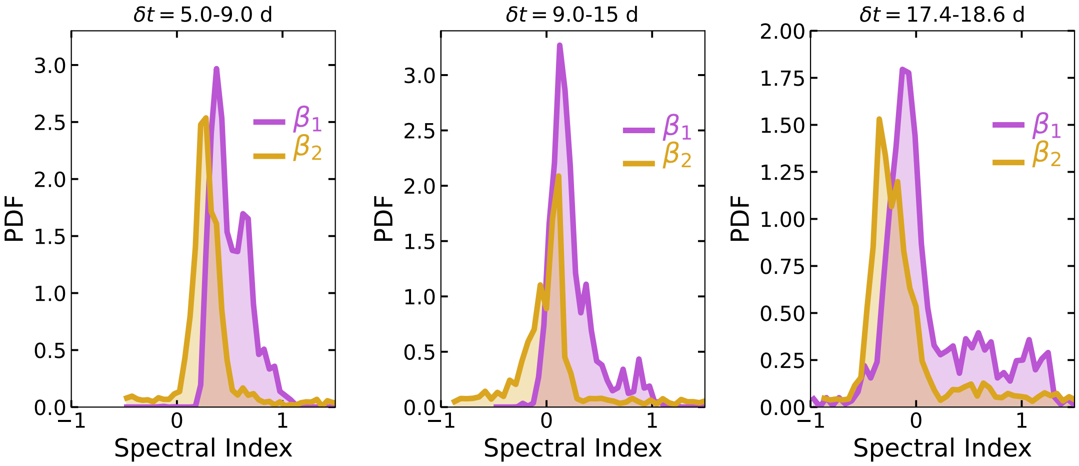

Figure 3. Probability density distributions of the spectral photon indices derived from the broadband X-ray spectral fitting of Section 4 with a BPL model. At the time of the flare peak at ≈50 days, we find evidence for a BPL spectrum with a rising spectrum $F_\nu \propto \nu^{1.25}$ at $h\nu \lesssim 8$ keV. There is a hint for a harder spectral index at softer energies at earlier times (i.e., $\beta_2 < \beta_1$), which suggests the presence of multiple spectral components, with the relative strength of the harder component increasing with time until the time of the flare peak (see Section 4.2).

We find that an SPL spectrum is a statistically acceptable description at all times, with the exception of the broadband X-ray spectrum acquired at the flare peak at $\delta t \approx 50$ days, when instead a BPL model is preferred. We list the best-fitting parameters, their uncertainties, and inferred fluxes in Table 1. We use the Goodman–Weare Markov Chain Monte Carlo (MCMC) implemented in `Xspec` with noninformative priors. For each fit, the chain length, number of walkers, and burn-in length were chosen to ensure convergence. Uncertainties are self-consistently derived with MCMC simulations. The spectral parameters of the favored model from this broadband analysis are then used to anchor the time-dependent flux calibration of the intermediate epochs with soft X-ray data only. For soft X-ray data acquired before the first NuSTAR epoch, the flux calibration is based on the best-fitting parameters from a Swift-XRT spectrum extracted at $\delta t = 2$–5 days in Table 1. The resulting unabsorbed 0.3–10 keV X-ray light curve of AT 2024wpp is shown in Figure 1.

AT 2024wpp shows luminous, roughly constant emission at the level of $L_{\rm x} \approx 1.5 \times 10^{43}$ erg s^{-1} in the first ≈7 days, followed by a phase of rapid decay with $L_{\rm x} \propto t^{-2.5\pm0.25}$ until $\delta t \approx 30$ days. Initially displaying a spectrum $F_\nu \propto \nu^{-\beta}$ with $\beta = 0.80^{+0.15}_{-0.16}$, the source spectrum later hardens with time and transitions into a *rising* $F_\nu \propto \nu^{-\beta}$ with $\beta < 0$ at ≈15 days (Figure 1, top panel). The source displays an episode of major rebrightening of X-rays starting at $\delta t \approx 35$ days and peaking at $\delta t \approx 50$ days, accompanied by extreme spectral hardening (soft X-ray spectrum $F_\nu \propto \nu^{1.25}$). At this time, the broadband X-ray spectrum is bell shaped, and it is best fit by a BPL model with break energy ≈8 keV and $F_\nu \propto \nu^{-1}$ above $E_{\rm break}$ (Figure 2). Remarkably, at ≈75 days, the soft X-ray spectrum is back to its initial, much softer state of $\beta = 0.60^{+0.17}_{-0.10}$ and remains consistent with this softer value until we can constrain the spectrum with XMM. This phenomenology is unprecedented among FBOTs but has clear physical connections with the Compton hump of AT 2018cow (R. Margutti et al. 2019) and possibly AT 2020mrf (Y. Yao et al. 2022), as we detail in Section 4.2.

Although an SPL model provides a statistically acceptable fit, a closer inspection of the best-fit parameters of the BPL model at $\delta t < 20$ days reveals that the soft X-rays are preferentially best fit by softer spectral indices than the hard X-rays (that is, $\beta_2 < \beta_1$ in Figure 3, where $F_\nu \propto \nu^{-\beta_1}$ for $\nu < \nu_{\rm break}$ and $F_\nu \propto \nu^{-\beta_2}$ above the break frequency $\nu_{\rm break}$). This observation opens the possibility that two emission components are contributing to the overall shape of the broadband X-ray spectrum, with the relative strength of the hard component increasing with time until the flare peak. We explore possible physical scenarios consistent with this possibility in Section 4.2.

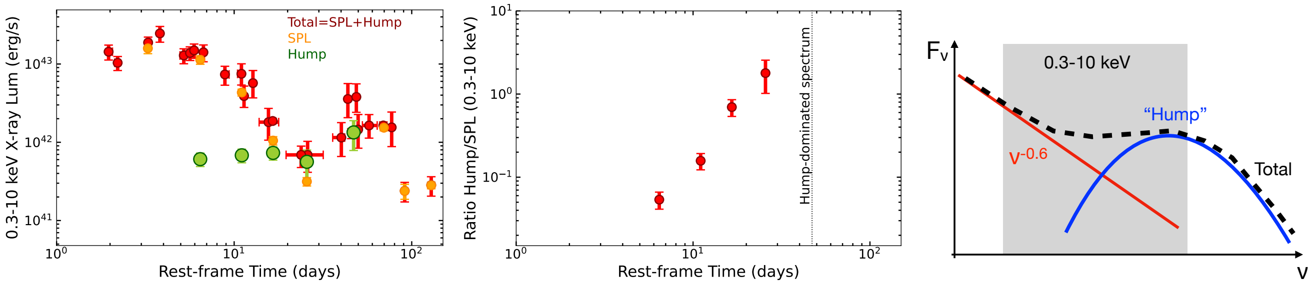

Figure 4. Evolution of the SPL (orange) and hump (lime green) component luminosities (left) and their ratio (middle) with time in the fixed observer-frame energy band 0.3–10 keV as constrained by our analysis of Section 4.2. The Compton hump contribution increases with time as the optical depth of the reprocessing layer decreases, causing the peak of the hump of emission (initially at >10 keV) to cascade to lower energies and enter the spectral window of interest (Figure 5). The hump dominates the 0.3–10 keV emission at $\delta t \approx 50$ days. Right: cartoon of the SPL+hump model showing how the progressive "emergence" of the hump of emission in the 0.3–10 keV band at $\delta t \leqslant 50$ days leads to hardening with time.

4.2. A Transient Compton Hump of Emission and Ionization Breakout

AT 2024wpp is the second LFBOT after AT 2018cow with clear evidence for a transient hump of emission. Compared with AT 2018cow (R. Margutti et al. 2019), the hump of X-ray emission in AT 2024wpp appears at a later time ($\delta t \approx 50$ days vs. ≈8 days) and with a lower peak energy ($E_{\rm break} \approx 8$ keV vs. ≈50 keV).[44] In both cases, after the hump disappears, the soft <10 keV X-ray spectrum reverts back to a spectral index value similar to the "pre-hump" phase $\beta \approx 0.5$–0.7. Motivated by the findings of Section 4.1, we explore an alternative set of fits for which we hypothesize that the observed X-ray spectrum is the superposition of an SPL ($F_\nu \propto \nu^{-\beta}$) and a hump component (here modeled with a BPL with slopes frozen to the values inferred for the $\delta t \approx 50$-day spectrum). For spectra at 5 days $< \delta t < 50$ days where hardening is apparent in the 0.3–10 keV band, we assume an SPL index $\beta = 0.6$. We fit for the normalization of each component (SPL, BPL) and for the free break energy. This approach allows us to explore the evolving contribution of a putative hump throughout this initial phase. Although this model is purely phenomenological and simplified, it is expected to capture the main properties of the evolution of the two components (displayed in Figure 4 in the fixed observer-frame 0.3–10 keV band). Figure 4 shows that the in-band contribution of the hump component grows with time, as is expected for a hump of emission with decreasing peak energy with time.

Physically, broadband X-ray spectra with similar properties and evolution are observed and expected in the case of transmission of radiation from a high-energy source through ejecta with time-variable optical depth to Compton scattering and photoelectric absorption, as was suggested for AT 2018cow (R. Margutti et al. 2019). In this scenario, the SPL represents the fraction of flux that is transmitted and reaches the observer unmodified, while the BPL mimics the combined results of Compton (down)scattering at the high photon-energy end and photoelectric absorption at lower energies. The BPL component dominates the 0.3–10 keV energy range as Thompson optical depth (τ_T) decreases (Figure 5). For $\tau_T \ll 1$ this model predicts that the 0.3–10 keV spectrum will eventually go back to its initial slope, as observed in both FBOTs.

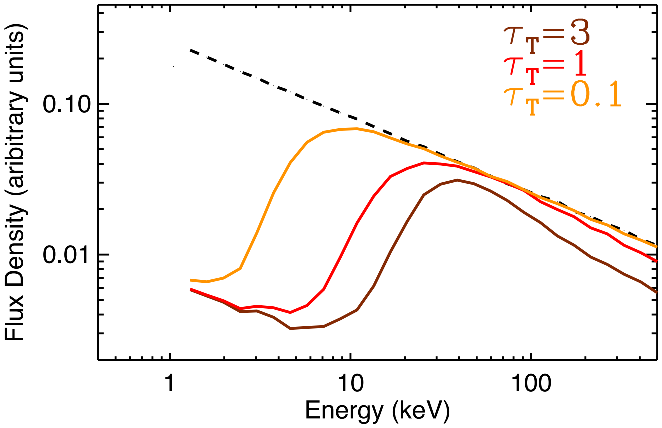

Figure 5. Selection of X-ray transmission spectra from a central source with intrinsic spectrum $F_\nu \propto \nu^{-0.5}$ (black dashed line) from the simulations presented in R. Margutti et al. (2019) for a range of Thomson optical depth values τ_T showing the increasing dominance of the Compton hump flux in the 0.3–10 keV band as τ_T decreases. These simulations do not account for time-dependent ionization effects in the transmission layer. See main text and R. Margutti et al. (2019) for more details on these simulations.

For AT 2018cow, at optical peak $\tau_T \sim (c/v_{\rm ej})(\kappa_{\rm es}/\kappa) \approx 20-40$, where $\kappa_{\rm es}$ is the electron scattering opacity, $v_{\rm ej}$ is the (optically emitting) ejecta velocity, and $\kappa_{\rm es} \approx 4\kappa$ was assumed (R. Margutti et al. 2019). In the absence of any other effect (e.g., continuous deposition of ejecta, or a change in the ionization state of the ejecta), the expansion of the ejecta leads to $\tau_T \propto t^{-2}$, implying $\tau_T \approx 3$ at the time of the prominent Compton hump at ≈8 days with an expected F_ν peak at ≈50 keV (Figure 5), consistent with observations (Figure 6 in R. Margutti et al. 2019). However, as discussed next, this reasoning does not apply to AT 2024wpp in this simple form, fundamentally because the observed $L_X/(L_X + L_{\rm UV\ OIR})$ ratio remains constant and $L_X/(L_X + L_{\rm UV\ OIR}) \approx L_X/L_{\rm UV\ OIR} \approx 10^{-2}$ during the first $\lesssim 20$ days, as opposed to steadily increasing with time as was observed in AT 2018cow (Paper I, Figure 9).

To quantitatively explore the implications of the observed evolution of the $L_X/(L_X + L_{\rm UV\ OIR})$ ratio, we adopt the parameterization of B. D. Metzger (2022). In this framework, the detected UV–optical–IR (UVOIR) luminosity is the result of reprocessing of a centrally located source of energy with luminosity $L_{\rm engine}$ by a two-component medium composed of slow-moving ejecta ($v \approx 6500\ {\rm km\ s^{-1}}$ inferred in Paper I) covering a fraction ϕ_0 of solid angle and fast-moving ejecta ($v \approx 0.2c$) subtending a solid angle $\Omega_{\rm fast} = 4\pi(1 - \phi_0)$. If the

---

[44] We note that a blueshifted Fe Kα feature such as the one detected in AT 2018cow would not be detectable against the continuum here because of the more limited statistics.

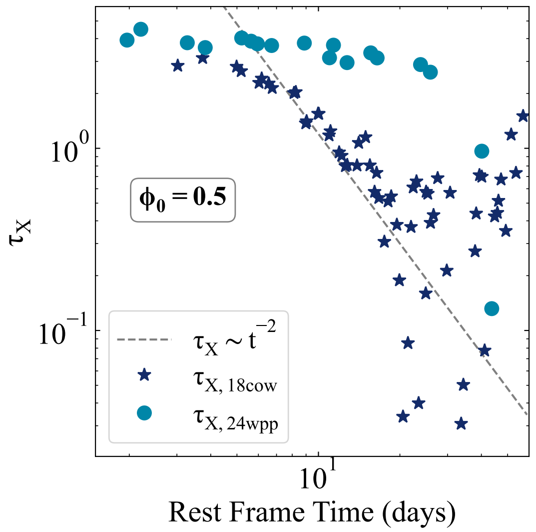

Figure 6. Effective optical depth to X-rays derived following the reprocessing model of B. D. Metzger (2022) and the observed X-ray and UVOIR emission for AT 2024wpp (filled circles) and AT 2018cow (stars). AT 2024wpp maintains higher τ_X for a significantly longer time, a behavior that is consistent with the delayed appearance of the Compton hump (Section 4.2). The gray dashed line shows $\tau_X \propto t^{-2}$ scaling expected for radiation shining through a medium expanding with constant velocity. We assume an arbitrary slow-moving ejecta covering fraction $\phi_0 = 0.5$.

slow-moving ejecta is completely opaque to X-rays, we expect $L_X = L_{\rm engine}(1-\phi_0)e^{-\tau_X}$, where we estimate $L_{\rm engine} \approx (L_X + L_{\rm UV\ OIR})$ and τ_X is the effective X-ray optical depth that we expect to roughly trace τ_T in an electron-scattering-dominated medium (as the probability of thermalization rapidly increases with the number of scatterings). From this reasoning, $L_X/(L_X + L_{\rm UV\,OIR}) \propto (1-\phi_0)e^{-\tau_X}$, or $L_X/L_{\rm UV\,OIR} \propto (1-\phi_0)e^{-\tau_X}$ for $L_X \ll L_{\rm UV\ OIR}$. The small and constant $L_X/L_{\rm UV\ OIR}$ ratio of AT 2024wpp thus implies large τ_X sustained for a long time (significantly longer than in AT 2018cow), as opposed to the expected $\propto t^{-2}$ behavior. We quantify this statement in Figure 6 for an arbitrary choice of $\phi_0 = 0.5$. Interestingly, $\tau_X \approx 0.1$ at $\delta t \sim 50$ days, for which Figure 5 predicts an F_ν peak energy of ≈8 keV as observed in AT 2024wpp (Figure 4).

Two considerations follow: (i) The delayed appearance of a Compton hump in AT 2024wpp is in line with (and should be expected based on) the large τ_X maintained until late times. We also note that the lower peak energy of the hump of emission in AT 2024wpp compared with AT 2018cow presumably originates from transmission through a medium with lower τ_T (Figures 5 and 6), which happens at a later epoch. (ii) τ_X clearly deviates from the $\propto t^{-2}$ evolution. (i)+(ii) can result from a variety of effects, including a time-variable level of ionization of the ejecta, which changes the opacity to X-rays (see below); continuous deposition of mass (as opposed to a one-time mass ejection); or a time-varying covering fraction ϕ_0 of the slow- versus fast-moving ejecta (e.g., as a consequence of different physical conditions of a super-Eddington accretion disk providing the source of ejecta mass).[45]

In the rest of this section we explore the possibility that the sudden drop of $\tau_X(t)$ at ≈40 days is due to an "ionization breakout," i.e., a reduction of the photoelectric absorption cross section resulting from the ionization of the ejecta by the inner source of energy. B. D. Metzger et al. (2014) and B. D. Metzger & A. L. Piro (2014) developed the theoretical framework in the context of magnetars formed by either stellar explosions or binary neutron star (NS) mergers, ionizing the surrounding ejecta with luminosity $L_{\rm ion}$, while D. Tsuna & W. Lu (2025) invoked an ionization breakout scenario in the context of FBOTs powered by accretion on newly formed NSs and black holes (BHs). Here we remain agnostic about the astrophysical nature of the ionizing luminosity $L_{\rm ion}$, and we consider a central engine ionizing the ejecta of mass $M_{\rm ej}$ expanding with velocity $v_{\rm ej}$ on a timescale t. Following B. D. Metzger et al. (2014), their Equations (A7) and (A11), we expect the radiation to ionize its way through the ejecta on a timescale

$$t_{\rm ion} \approx \begin{cases} 30\ {\rm days}\ M_2^{3/4}\left(\dfrac{v_{\rm ej}}{0.2c}\right)^{-5/4} T_5^{-0.2}\left(\dfrac{X_Z}{0.5}\right)^{1/4}\left(\dfrac{Lt}{5\times10^{50}}\right)^{-1/4} Z_8^{3/4} \\ (\eta_{\rm thr} \ll 1), \\ 50\ {\rm days}\ M_2\left(\dfrac{v_{\rm ej}}{0.2c}\right)^{-3/2} T_5^{-0.4}\left(\dfrac{X_Z}{0.5}\right)^{1/2}\left(\dfrac{Lt}{5\times10^{50}}\right)^{-1/2} Z_8^{3/2} \\ (\eta_{\rm thr} \gg 1), \end{cases} \tag{1}$$

where $M_2 \equiv M_{\rm ej}/(2\ M_\odot)$, $T_5 \equiv T/10^5$ K is the temperature of electrons in the recombination layer, X_Z is the mass fraction of elements with atomic number $Z = 8Z_8$ in the ejecta, and

$$\eta_{\rm thr} \approx 7.5\left(\frac{Lt}{5\times10^{50}\ {\rm erg}}\right)^{-1} M_2\left(\frac{v_{\rm ej}}{0.2c}\right)^{-1} \times \left(\frac{X_Z}{0.5}\right) T_5^{-0.8} Z_8^3 \tag{2}$$

is the ratio of absorptive to scattering opacity in the ejecta. We have renormalized Equations (1) and (2) using parameter values that are relevant to the fast ejecta component of AT 2024wpp as constrained by optical and X-ray observations. For oxygen-dominated ejecta,[46] we find $t_{\rm ion} \approx 30$–50 days, which compares well with when the ejecta becomes transparent to the X-rays (and the hump dominates in the 0.3–10 keV energy range). While our analytical arguments require confirmation by detailed simulations in future work, based on the calculations above, we consider it plausible that the $\tau_X(t)$ drop is at least partially driven by ionization effects.

To conclude, in close analogy with AT 2018cow (R. Margutti et al. 2019), our broadband X-ray analysis favors the presence of a highly variable, centrally located high-energy source shining through expanding aspherical ejecta material with time-dependent ionization (and potentially covering fraction). We address the astrophysical nature of the high-energy source in the next section.

---

[45] We note that at face value the smaller $L_X/(L_X + L_{\rm UV\ \ OIR})$ ratio of AT 2024wpp compared with AT 2018cow can be interpreted as a larger covering fraction ϕ_0, leading to a larger fraction of engine luminosity being reprocessed in UVOIR emission.

[46] We note that lighter elements would be ionized significantly earlier, consistent with the lack of spectral features at early times; instead, the slower-moving ejecta would be opaque to X-ray radiation for much longer. We also note that Equation (1) does not account for the possible ongoing deposition of mass, which would delay the emergence of the ionization front compared to the estimate presented above.

4.3. The Soft X-Ray Spectral Index and the Origin of the X-Ray Emission

AT 2018cow–like FBOTs display similar values of the soft X-ray spectral index of the persistent component (i.e., the component *not* associated with the Compton hump) $F_\nu \propto \nu^{-\beta}$ with $\beta \approx 0.6$. As was noted for AT 2018cow (R. Margutti et al. 2019), this hard spectrum maintained over tens of days is not compatible with fast cooling of the radiating electrons for any reasonable values of the electron energy distribution index $p \gtrsim 2$ (where $N(E) \propto E^{-p}$). Together with the initial X-ray light-curve plateau followed by a steep temporal decay, prominent X-ray variability with increasing variance with time, and the Compton hump spectrum, this hard spectral index might be a defining trait of this class of transients. From an observational perspective, we note that the $F_\nu \propto \nu^{1.26}$ emission component is harder than the typical power-law component of X-ray binaries (XRBs) and active galactic nuclei (AGNs), which is often attributed to Comptonization of soft disk photons (e.g., L. Titarchuk & E. Seifina 2021, and references therein). Additionally, similar to AT 2018cow, the X-ray emission and radio emission are not part of the same synchrotron spectrum at any time (the X-rays being always brighter than the extrapolated radio spectrum). Following the same line of reasoning as in R. Margutti et al. (2019, their Section 3) for AT 2018cow that we do not repeat here, we find that these observations imply the presence of an inner, highly variable source capable of continuously "heating" the radiating electrons to maintain the slow-cooling spectrum.

Magnetic reconnection (e.g., in a magnetar nebula or accreting BH corona) or the dissipation of outflow kinetic energy (e.g., via internal shocks between multiple episodes of accretion disk wind or bulk Comptonization) could in principle satisfy these requirements.

GMRHD simulations of super-Eddington accreting disks (A. Sadowski & R. Narayan 2015, 2016) reveal the generation of powerful outflows reaching transrelativistic velocities along the polar direction and carrying a total (i.e., radiative and kinetic) luminosity $L \sim \eta \dot{M}_\bullet c^2$ with $\eta \sim 0.03$ for a nonrotating ($a = 0$) stellar-mass BH (for $a = 0.7$, $\eta \sim 0.08$). Simulations by A. Sadowski & R. Narayan (2016) extended to accretion rates up to a few hundred $\dot{M}_{\rm Edd}$, which is $\approx 10^3$ times smaller than what is needed to power FBOTs at peak, finding that at high $\dot{M}$ most of the outflow luminosity is in the kinetic form.[47] Building on the results from these simulations and extrapolating to significantly higher accretion rates, B. D. Metzger (2022) and D. Tsuna & W. Lu (2025) demonstrated how stellar-mass BHs accreting at highly super-Eddington rates produce outflows that can carry enough kinetic energy $E_k > 10^{51}$ erg to match the (extreme) energetic requirements and timescales of FBOTs like AT 2024wpp (see their Equations (18) and (37), respectively). It is important to note that the astrophysical context of the two models is different: a tidal disruption and hyperaccretion of a Wolf–Rayet (W-R) star by a BH or NS binary companion are invoked by B. D. Metzger (2022), versus the collision of a newly formed NS or BH from a CCSN explosion with its main-sequence companion by D. Tsuna & W. Lu (2025). However, both models share the common ingredient of super-Eddington accretion on a compact object and directly connect the FBOT phenomenology to the dissipation of energy carried by the resulting outflows.

To conclude, we thus consider the likely possible origins for the central X-ray source: (i) a pulsar-wind-nebula-like system, i.e., a magnetized nebula energized by a compact object (e.g., I. Vurm & B. D. Metzger 2021); and (ii) emission related to super-Eddington accretion disks around compact objects. Both systems can power collimated jets (for which we have no direct observational evidence in FBOTs) as proposed by O. Gottlieb et al. (2022). More generally, irrespective of the details of the astrophysical origin of the X-ray source, the X-ray emission in FBOTs likely escapes from a lower-density polar region, which in all likelihood implies geometrical beaming. This fact has two observational consequences: first, the "true" X-ray luminosity from the system is lower than what is estimated assuming isotropic emission ($L_{\rm true} = L_{\rm iso} \times \Delta\Omega/4\pi$).[48] Second, geometrical beaming implies a viewing angle dependency of the observed $L_{\rm x}$ (with observing angles aligned with the polar direction being associated with the brighter displays at early times), which might be at the core of the range of X-ray luminosity behaviors observed in LFBOTs (discussed in detail in Section 7.2), as well as the appearance and prominence of the Compton hump.

5. Radio Modeling and Inferences

5.1. General Considerations

Radio emission from FBOTs is understood to originate from the shock interaction with the surrounding medium (A. Y. Q. Ho et al. 2019, 2022; R. Margutti et al. 2019; D. L. Coppejans et al. 2020; J. S. Bright et al. 2022; Y. Yao et al. 2022; A. A. Chrimes et al. 2024a). The resulting radio spectral energy distributions (SEDs) are bell shaped, where the peak is due to synchrotron self-absorption (SSA) of relativistic electrons accelerated at the shock front to a power-law distribution of the form $N(E) \propto E^{-p}$ down to a minimum Lorentz factor γ_m (R. A. Chevalier 1998). In a standard SSA scenario, the optically thick spectral index is $\alpha_2 = 5/2$ (with $F_\nu \propto \nu^{\alpha_2}$) and the optically thin spectral index is $\alpha_1 = -(p-1)/2$ (with $F_\nu \propto \nu^{\alpha_1}$). If synchrotron-emitting electrons are efficiently cooled via synchrotron or inverse Compton (IC) emission, the optically thin spectral index above the cooling frequency ν_c becomes $\alpha_1 = -p/2$. As the shock propagates in the surrounding medium of the density profile $\rho \propto r^{-k}$, the SSA spectral peak shifts to lower frequencies. For a wind-like circumstellar medium (CSM) density profile (i.e., $k = 2$), $\nu_{\rm pk} \propto t^{-1}$ while $F_{\rm pk}$ remains constant.

Figure 7 shows the radio SEDs of AT 2024wpp at $\delta t_{\rm rest} \approx 13$–161 days. Although the shapes of the SEDs are similar to the one expected from SSA emission, the evolution of the SEDs is nonstandard. The peak flux density of the SEDs brightens by approximately a factor of 10 between $\delta t_{\rm rest} \approx 17$ and 32 days. Subsequently, at $\delta t_{\rm rest} \approx 46$–73 days, the peak flux remains roughly constant, with the peak frequency moving to lower frequencies, followed by a decrease in $\nu_{\rm pk}$ and $F_{\rm pk}$ at $\delta t_{\rm rest} \approx 118$ days. The optically thick phase of the spectrum is best sampled at $\delta t_{\rm rest} \approx 32$ days, and the spectral index is $\alpha_2 \approx 0.7$. The slope is slightly steeper at $\delta t_{\rm rest} \approx 46$ days, $\alpha_2 \approx 1.5$. In either case, the optically thick spectral indices are flatter than that expected from SSA ($\alpha_2 = 2.5$). This deviation

---

[47] Recent results from a wider range of non-MHD simulations by S. Yoshioka et al. (2024) confirm these findings.

[48] Similar arguments have been used to explain the super-Eddington X-ray luminosity of ultraluminous X-ray sources (see, e.g., A. King et al. 2023).

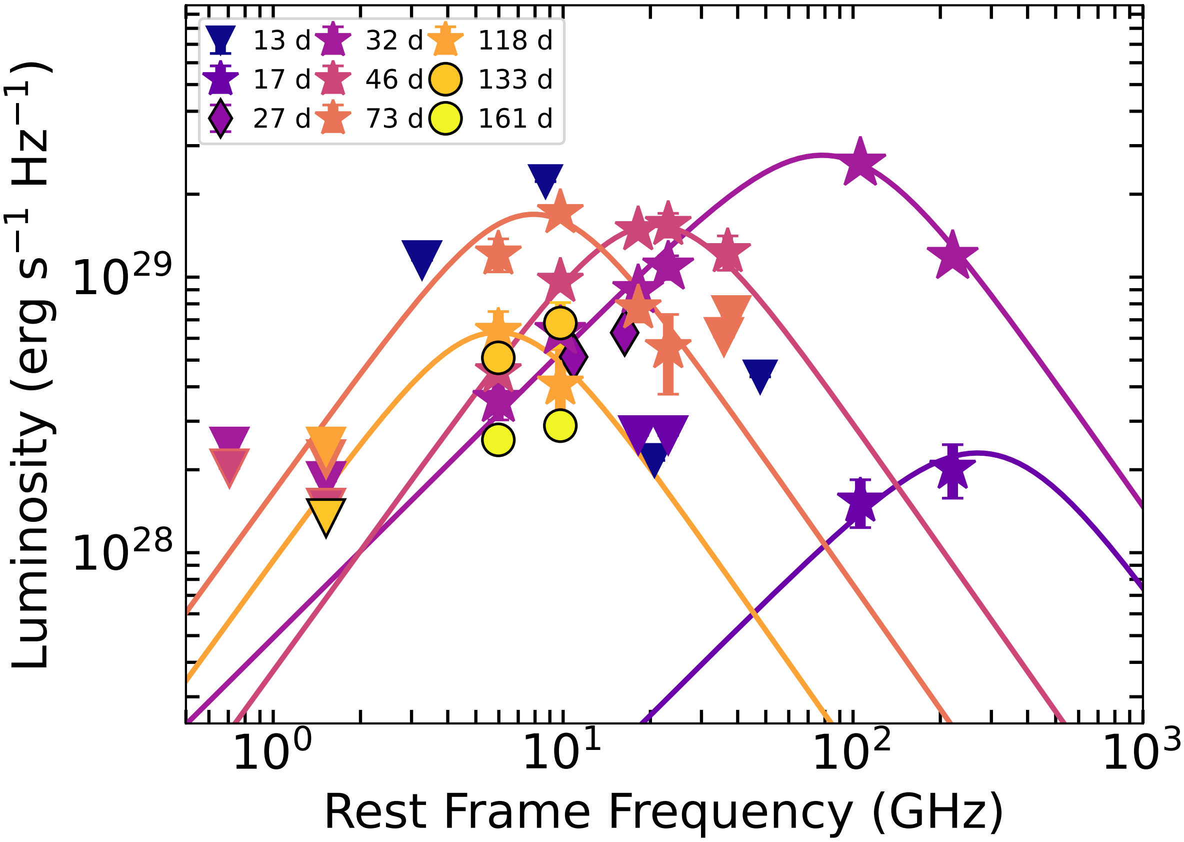

Figure 7. Radio spectra of AT 2024wpp in the time range $\delta t_{\rm rest} \approx$ 13–161 days acquired with MeerKAT, GMRT, ATCA, ATA, and ALMA. The purple diamonds denote the VLA flux measurements from G. Schroeder et al. (2024). Inverted triangles mark the 3σ flux density upper limits. Solid lines represent best-fit BPL models with smoothing parameter $s = -1$ and optically thin spectral index $\alpha_1 = -1.5$. AT 2024wpp shows a complex evolution with two unprecedented elements: (i) an extremely rapid and delayed rise of the millimeter emission captured by ALMA, and (ii) radio spectrum inversion in the last two ATCA epochs (emphasized with circles).

is commonly observed in LFBOTs (A. Y. Q. Ho et al. 2019, 2022, 2023b; R. Margutti et al. 2019; J. S. Bright et al. 2022; A. J. Nayana & P. Chandra 2021) and is often attributed to inhomogeneities in the emitting region (K. W. Weiler et al. 2002; C. I. Björnsson & S. T. Keshavarzi 2017; C. I. Björnsson 2024). The optically thin slope is $\alpha_1 \approx -1$ at $\delta t \approx 73$ days, implying $p \approx 3$. We thus adopt $p \approx 3$ for synchrotron spectral modeling and parameter estimation.

The spectral behavior at $\delta t_{\rm rest} > 118$ days is particularly striking. The spectral peak is $\nu_{\rm pk} \approx 6$ GHz, with a 5–9 GHz spectral slope of $\alpha_1 = -0.90 \pm 0.78$. In later observations, we find evidence for a spectral inversion at these frequencies (5–9 GHz), with $\alpha_1 = 0.59 \pm 0.31$ and 0.24 ± 0.50 at 133 and 161 days, respectively (A. J. Nayana et al. 2025). This kind of spectral inversion is unprecedented in FBOTs and may signal the emergence of a new emission component.

5.2. Spectral Modeling and Shock Parameters

We model the single-epoch SEDs of AT 2024wpp as a BPL of the form

$$F_\nu = F_{\rm pk}\left[\left(\frac{\nu}{\nu_{\rm pk}}\right)^{\alpha_1/s} + \left(\frac{\nu}{\nu_{\rm pk}}\right)^{\alpha_2/s}\right]^s, \tag{3}$$

where α_1 and α_2 denote the optically thin and thick spectral slopes, respectively, and s defines the smoothness of the BPLs. We fix $\alpha_1 = -1.5$ and $s = -1$ while keeping $F_{\rm pk}$ and $\nu_{\rm pk}$ as free parameters. We choose $\alpha_1 = -1.5$ based on the optically thin spectral index at $\delta t_{\rm rest} \approx 73$ days and the position of cooling frequencies, which are self-consistently calculated later in this section. At $\delta t_{\rm rest} \approx 17$ and 32 days the cooling frequencies are below the SED peak, while at $\delta t_{\rm rest} \approx 46$ days it is closer to the peak. This would result in a steepening in the optically thin spectral slope by $\Delta\alpha = 0.5$, and the optically thin slope at $\delta t_{\rm rest} \approx 73$ days is ≈ -1. In addition, we keep α_2 as a free parameter at $\delta t_{\rm rest} \approx 32$ and 46 days. At other epochs, we fix α_2 to the best-fit values obtained in the nearest-epoch SED.

Following R. A. Chevalier (1998), we calculate the shock radius (R) and magnetic field (B) for $p = 3$ using the following equations:

$$R = 8.8 \times 10^{15} f_{\rm eB}^{-1/19}\left(\frac{f}{0.5}\right)^{-1/19}\left(\frac{F_{\rm pk}}{\rm Jy}\right)^{9/19} \tag{4}$$

$$\times \left(\frac{D}{\rm Mpc}\right)^{18/19}\left(\frac{\nu_{\rm pk}}{\rm GHz}\right)^{-1} {\rm cm} \tag{5}$$

$$B = 0.58 f_{\rm eB}^{-4/19}\left(\frac{f}{0.5}\right)^{-4/19}\left(\frac{F_{\rm pk}}{\rm Jy}\right)^{-2/19}$$

$$\times \left(\frac{D}{\rm Mpc}\right)^{-4/19}\left(\frac{\nu_{\rm pk}}{5\ {\rm GHz}}\right) {\rm G}. \tag{6}$$

Table 2
Shock Parameters of AT 2024wpp Estimated from Single-epoch Radio Spectral Modeling

Time[a] (days)	α_2	$\nu_{\rm pk}$[b] (GHz)	$F_{\rm pk}$[b] (mJy)	R ($\times 10^{16}$ cm)	$(\Gamma\beta)c$[c] (c)	B (Gauss)	n (cm^{-3})	U ($\times 10^{48}$ erg)
17.5[d]	1.05	310^{+123}_{-98}	$0.224^{+0.058}_{-0.045}$	$0.06^{+0.02}_{-0.01}$	$0.013^{+0.004}_{-0.002}$	$36.9^{+24.4}_{-16.6}$	$6.42^{+1.9}_{-0.5} \times 10^8$	$0.07^{+0.04}_{-0.03}$
32.4	$1.05^{+0.05}_{-0.05}$	90^{+5}_{-5}	$2.697^{+0.077}_{-0.069}$	$0.56^{+0.03}_{-0.03}$	$0.067^{+0.004}_{-0.004}$	$4.1^{+0.4}_{-0.4}$	$0.31^{+0.09}_{-0.07} \times 10^6$	$0.76^{+0.01}_{-0.01}$
46.1	$1.45^{+0.18}_{-0.16}$	21^{+3}_{-2}	$1.524^{+0.062}_{-0.052}$	$2.91^{+0.36}_{-0.36}$	$0.244^{+0.03}_{-0.03}$	$1.3^{+0.2}_{0.2}$	$2.5^{+1.8}_{-0.9} \times 10^3$	$11.44^{+1.33}_{1.33}$
72.7	1.45	$8^{+0.5}_{-0.5}$	$1.673^{+0.074}_{-0.068}$	$7.88^{+0.65}_{-0.56}$	$0.418^{+0.035}_{-0.030}$	$0.5^{+0.03}_{-0.03}$	$1.23^{+0.38}_{-0.31} \times 10^2$	$33.12^{+3.77}_{-3.10}$
117.6	1.45	6^{+4}_{-2}	$0.624^{+0.159}_{-0.112}$	$6.04^{+2.87}_{-2.23}$	$0.198^{+0.094}_{-0.073}$	$0.4^{+0.3}_{-0.1}$	$4.2^{+4.6}_{-0.3} \times 10^2$	$11.68^{+7.6}_{-3.9}$

Notes.

[a] With respect to date of first light in rest frame $\delta t_{\rm rest} = \delta t_{\rm obs}/(1 + z)$.

[b] $\nu_{\rm pk}$ and $F_{\rm pk}$ are the intersection of the optically thick and thin power laws of synchrotron spectrum. The parameters are estimated assuming equipartition ($\epsilon_e = \epsilon_B = 0.33$).

[c] Mean shock velocity $(\Gamma\beta)c = Rc/t$.

[d] The parameters at $\delta t_{\rm rest} \approx 17.5$ days are not physical, as the SED is free–free absorbed owing to the surrounding medium up to radius $R \approx 10^{16}$ cm (see Section 6.3).

The shock internal energy (U) is given by

$$U = \frac{1}{\epsilon_B}\frac{4}{3}\pi f R^3 \frac{B^2}{8\pi}. \tag{7}$$

Here $f_{\rm eB} \equiv \frac{\epsilon_e}{\epsilon_B}$, where ϵ_e and ϵ_B are the fractions of post-shock energy in the relativistic electrons and magnetic fields, respectively. We assume equipartition of energy, i.e., $f_{\rm eB} = 1$ (for $\epsilon_{\rm e} = \epsilon_{\rm B} = 0.3$). Parameter f is the volume filling factor of the synchrotron-emitting region and is taken to be $f = 0.5$ (R. A. Chevalier 1998).

The R. A. Chevalier (1998) model assumes that the cooling frequency (ν_c) is above the SSA frequency (ν_a) and that the synchrotron characteristic frequency emitted by minimum energy electrons (ν_m) is below ν_a (i.e., $\nu_m < \nu_a < \nu_c$). This order of characteristic frequencies may not be valid at all times. For example, in AT 2018cow, $\nu_a > \nu_c$ at early times, due to the presence of a dense medium in the immediate environment, and shock energy was dissipated in a small volume (A. Y. Q. Ho et al. 2019).

We calculate ν_m and cooling frequencies (both synchrotron cooling frequency, $\nu_{c,{\rm sync}}$, and IC cooling frequency, $\nu_{c,{\rm IC}}$) at different epochs to check the validity of this model. The minimum Lorentz factor (γ_m) of a distribution of accelerated electrons of energy power-law index p is given by $\gamma_m = \frac{p-2}{p-1}\frac{m_p}{m_e}\epsilon_e\beta^2$, where β is the shock velocity in units of c. The corresponding minimum characteristic synchrotron frequency is $\nu_m = \gamma_m^2\nu_g$, where $\nu_g = \frac{qB}{2\pi m_e c}$ is the gyrofrequency. Here q and m_e are the charge and mass of the electron, respectively. We find $\nu_m \ll \nu_{\rm pk} \equiv \nu_a$ during the observed epochs. The synchrotron and IC cooling frequencies are $\nu_{c,{\rm sync}} = \gamma_{\rm sync}^2\nu_g$ and $\nu_{c,{\rm IC}} = \gamma_{\rm IC}^2\nu_g$, respectively, where electrons with $\gamma > \gamma_{\rm sync}$ or $\gamma_{\rm IC}$ cool at time t. Parameters $\gamma_{\rm sync}$ and $\gamma_{\rm IC}$ are given by (G. B. Rybicki & A. P. Lightman 1979)

$$\gamma_{\rm sync} = \frac{6\pi mc^2}{\sigma_{\rm T} cB^2 t} \tag{8}$$

$$\gamma_{\rm IC} = \frac{3\pi mc^2R^2}{\sigma_{\rm T} L_{\rm bol} t}. \tag{9}$$

Here $\sigma_{\rm T}$ is the Thomson scattering cross section and $L_{\rm bol}$ is the bolometric luminosity at time t. We calculate $\nu_{c,{\rm sync}}$ and $\nu_{c,{\rm IC}}$ using R and B from Table 2. We use $L_{\rm bol} \approx (8, 0.9, 0.3, 0.07, 0.01) \times 10^{43}$ erg s^{-1} at $\delta t_{\rm rest} =$ 17.5, 32.4, 46.1, 72.7, and 117.6 days, respectively (Paper I). The cooling frequencies are lower than $\nu_{\rm pk}$ at $\delta t_{\rm rest} =$ 17.5 and 32.4 days, which implies that R. A. Chevalier (1998) is not self-consistent at these epochs. A. Y. Q. Ho et al. (2022) present formulae to estimate source properties in the regime $\nu_a > \nu_c$ (see their Appendix C). For $p = 3$, the expressions for R and B are as follows:

$$R = 4.2 \times 10^{15} f_{\rm eB}^{-1/13}\left(\frac{F_{\rm pk}}{\rm Jy}\right)^{6/13}\left(\frac{D}{\rm Mpc}\right)^{12/13} \times \left(\frac{\nu_{\rm pk}}{\rm GHz}\right)^{-11/13}\left(\frac{t}{100\ {\rm days}}\right)^{1/13} {\rm cm} \tag{10}$$

$$B = 0.14 f_{\rm eB}^{-4/13}\left(\frac{F_{\rm pk}}{\rm Jy}\right)^{-2/13}\left(\frac{D}{\rm Mpc}\right)^{-4/13} \times \left(\frac{\nu_{\rm pk}}{5\ {\rm GHz}}\right)^{21/13}\left(\frac{t}{100\ {\rm days}}\right)^{4/13} {\rm G}. \tag{11}$$

We estimate shock parameters at $\delta t_{\rm rest} \approx 17$ and 32 days using these equations and report the self-consistent estimates of R, v, B, U, and n at all epochs in Table 2. We note that the parameters at $\delta t_{\rm rest} \approx 17.5$ days are not physical, as the SED at $\delta t_{\rm rest} \approx 17$ days is free–free absorbed owing to the surrounding medium up to radius $R \approx 10^{16}$ cm. The SED evolution between $\delta t_{\rm rest} \approx 17$ and 32 days is best explained in a scenario where the shock is propagating through a dense shell (see Section 6.3).

5.3. Synchrotron Emission from Thermal Electrons

Collisionless strong shocks are commonly believed to accelerate electrons into a nonthermal power-law distribution via diffusive shock acceleration (A. R. Bell 1978; R. D. Blandford & J. P. Ostriker 1978; R. Blandford & D. Eichler 1987; A. Spitkovsky 2008; L. Sironi & A. Spitkovsky 2009, 2011; D. Caprioli 2015). Numerical models of collisionless shocks suggest that the electron distribution consists of both thermal and nonthermal populations. B. Margalit & E. Quataert (2021) discuss the contribution of thermal electrons to the emergent synchrotron flux in transrelativistic shocks and find a significant contribution from thermal electrons toward the peak emission for shocks of velocity $v \gtrsim 0.2c$. The key observational signatures of synchrotron emission from thermal electrons are a steep optically thin spectral index and an $F_\nu \propto \nu^2$ spectral slope in the optically thick regime.

A. Y. Q. Ho et al. (2022) reported a steep optically thin spectral index $\alpha_1 \approx -2$ in the case of AT 2020xnd and modeled the SEDs as synchrotron emission from a thermal population of electrons. The observed optically thin spectral index for AT 2024wpp is $\alpha_1 = -1.29 \pm 0.17$, with an optically thick spectral slope of $\alpha_2 = 0.66 \pm 0.02$ ($\delta t_{\rm rest} \approx 32$ days) and $\alpha_2 = 1.45 \pm 0.18$ ($\delta t_{\rm rest} \approx 46$ days). The shock velocities from single-epoch spectral modeling are $v > 0.2c$ at $\delta t_{\rm rest} \approx 46$ and 73 days (see Table 2). Even though the spectral slope is not as steep as that expected from a thermal population, motivated by the large shock velocities, we fit individual SEDs at $\delta t_{\rm rest} \approx$ 32, 46, and 73 days with the "thermal + nonthermal" synchrotron emission model of B. Margalit & E. Quataert (2021) and explore the parameter space using MCMC. We keep the number density, shock radius, and electron thermalization efficiency (ϵ_T) as free parameters and run the fit, keeping the ratio of energy in nonthermal electrons to thermal electrons ($\delta = \epsilon_e/\epsilon_T$) and ϵ_B fixed. We use $\epsilon_B = 0.1$ and run the model for a range of δ values ($\delta = 0.001$, 0.01, 0.1, and 1). The model failed to reproduce the SEDs at $\delta t_{\rm rest} \approx$ 32 and 46 days but resulted in reasonable fits for $\delta t_{\rm rest} \approx 73$ days. The model resulted in optically thick spectral slopes that were too steep and could not match the observed values at $\delta t_{\rm rest} \approx 32$ days. At $\delta t_{\rm rest} \approx 46$ days, the peak and decay were not reproduced by the models. The best-fit values of parameters at $\delta t_{\rm rest} \approx 73$ days are $R = 7.13^{+0.91}_{-0.67} \times 10^{16}$ cm, $n = 129^{+32}_{-27}$ cm^{-3}, and $\epsilon_T = 0.56^{+0.28}_{-0.21}$ for $\epsilon_B = 0.1$ and $\delta = 0.1$ (i.e., $\epsilon_e = 0.005$). The shock radius and density derived from this model are very similar to the ones estimated from single-epoch spectral modeling as expected (see Figure 2 of B. Margalit & E. Quataert 2021, Section 4) and also seen in the case of AT 2020xnd (A. Y. Q. Ho et al. 2022). Although there may be some contribution to the synchrotron flux of thermal electrons at $\delta t_{\rm rest} \approx 73$ days, we conclude that it is not necessary to invoke this model to interpret the observed SEDs.

6. The Origin and Evolution of the Radio-emitting Outflow

The spectral evolution of AT 2024wpp is characterized by distinct phases in the time evolution of both the peak flux density and peak frequency. The peak flux density increases as $F_{\rm pk} \propto t^{4.04\pm0.42}$ during $\delta t_{\rm rest} \approx$ 17–32 days. This is followed by a slight decline between 32 and 73 days ($F_{\rm pk} \propto t^{-0.67\pm0.06}$) and a steeper decay as $F_{\rm pk} \propto t^{-2.05\pm0.54}$ at $\delta t_{\rm rest} > 73$ days. The corresponding evolution of the peak frequency is $\nu_{\rm pk} \propto t^{-2.01\pm0.65}$ at $\delta t_{\rm rest} \approx$ 17–32 days, $\nu_{\rm pk} \propto t^{-2.99\pm0.10}$ at $\delta t_{\rm rest} \approx$ 32–73 days, and $\nu_{\rm pk} \propto t^{-0.60\pm1.05}$ at $\delta t_{\rm rest} \approx$ 73–118 days. The rapid brightening of SEDs between $\delta t_{\rm rest} \approx 17$ and 32 days may be attributed to suppression of the intrinsic synchrotron emission due to radiative cooling processes (IC and/or synchrotron cooling). In particular, depending on the position of the cooling frequency, the cooling process can reduce the observable flux at early epochs. We investigate the relative importance of different cooling processes to explain the observed SED evolution in Section 6.1.

The physical parameters inferred from single-epoch spectral analysis imply a rapidly growing radio-emitting region, with a temporal evolution of $R \propto t^{3.12\pm0.12}$, consistent with an accelerating outflow. The outflow velocity increases from $\Gamma\beta c \approx 0.07c$ to $0.42c$ during $\delta t_{\rm rest} =$ 32–73 days, with an increasing amount of internal energy coupled to this outflow (see Table 2). The increase in the blast wave energy with time and its acceleration can be (i) intrinsic or (ii) apparent. If intrinsic, more energy is being deposited into the shock with time (e.g., via continuous winds from an accretion disk). The shock then breaks out from this dense region and accelerates in a very steep density profile, a process similar to that of shocks expanding in the outer layers of exploding massive stars. Alternatively, if the effect is apparent, such evolution can arise as a result of geometric effects. In off-axis jet models, the observer sees more energy progressively coming into their line of sight as a consequence of the deceleration of the outflow. We explore both scenarios in detail in Sections 6.2 and 6.3.

6.1. Energy Losses of Synchrotron-emitting Electrons

Synchrotron-emitting electrons can lose energy via various cooling processes: synchrotron cooling and/or IC cooling. In synchrotron cooling, relativistic electrons lose energy by emitting radiation in the presence of magnetic fields, with the cooling efficiency increasing at higher magnetic field strengths and electron energies. In the presence of a strong radiation field, relativistic electrons can upscatter low-energy optical photons to higher energies and IC cooling can be important. The millimeter emission from AT 2024wpp at $\delta t_{\rm rest} \approx 17$ days is an order of magnitude lower than the millimeter emission at $\delta t_{\rm rest} \approx 32$ days. We explore the possibility of flux suppression via electron cooling to account for this. In the case of an IC cooling scenario, the radio outflow needs to always be in front of the optical photosphere. We plot the optical and radio photosphere radii of AT 2024wpp at multiple epochs ($\delta t_{\rm rest} \approx$ 32–118 days) in the right panel of Figure 8 and find that this is indeed the case.

We extrapolate the radio SED from $\delta t_{\rm rest} \approx 46.1$ days to $\delta t_{\rm rest} \approx 17.5$ days assuming a density profile $\rho_{\rm CSM} \propto r^{-3}$ and a constant shock velocity of $\Gamma\beta c = 0.24c$. The expected flux densities at 100 and 200 GHz on this SED are ≈ 3.1 and 1.6 mJy, respectively. At this epoch, the Lorentz factor of electrons cooling via IC cooling is $\gamma_{\rm IC} = 12$, and that via synchrotron cooling is $\gamma_{\rm sync} = 14$ (for $\epsilon_e = \epsilon_B = 0.3$), indicating that IC cooling is marginally dominant. The Lorentz factors of electrons emitting at 100 and 200 GHz are ≈ 117 and 166, respectively, at $\delta t_{\rm rest} \approx 17.5$ days. Thus, cooling can suppress the flux at 100 GHz by a factor of ≈10 and at 200 GHz by a factor of ≈14. This will result in observed flux densities of $F_{100\,{\rm GHz}} \approx 0.3$ mJy and $F_{200\,{\rm GHz}} \approx 0.1$ mJy. The observed ALMA flux densities at $\delta t_{\rm rest} \approx 17.5$ days are $F_{100\,{\rm GHz}} = 0.08$ mJy and $F_{200\,{\rm GHz}} = 0.10$ mJy, which are ≈4 times lower at 100 GHz and similar at 200 GHz. Hence, the ALMA flux densities are suppressed beyond what can be accounted for by electron cooling alone at 100 GHz, whereas at 200 GHz the flux density is consistent with that expected from IC suppression.

If we carry out a similar exercise by extrapolating the synchrotron SED from $\delta t_{\rm rest} \approx 46.1$ days to $\delta t_{\rm rest} \approx 32.4$ days, the Lorentz factor of electrons experiencing IC cooling is ≈203 and that for synchrotron cooling is ≈49, indicating that synchrotron cooling is the dominant cooling process. The effect of cooling should suppress the flux to $F_{100\,{\rm GHz}} \approx 0.15$ mJy and $F_{200\,{\rm GHz}} \approx 0.04$ mJy. However, the observed flux densities at $\delta t_{\rm rest} \approx 32.4$ days are $F = 1.3$ mJy at 100 GHz and $F = 0.6$ mJy at 200 GHz, which are 9–15 times higher.

We caution that the above estimates based on cooling timescales depend strongly on the CSM density profile and

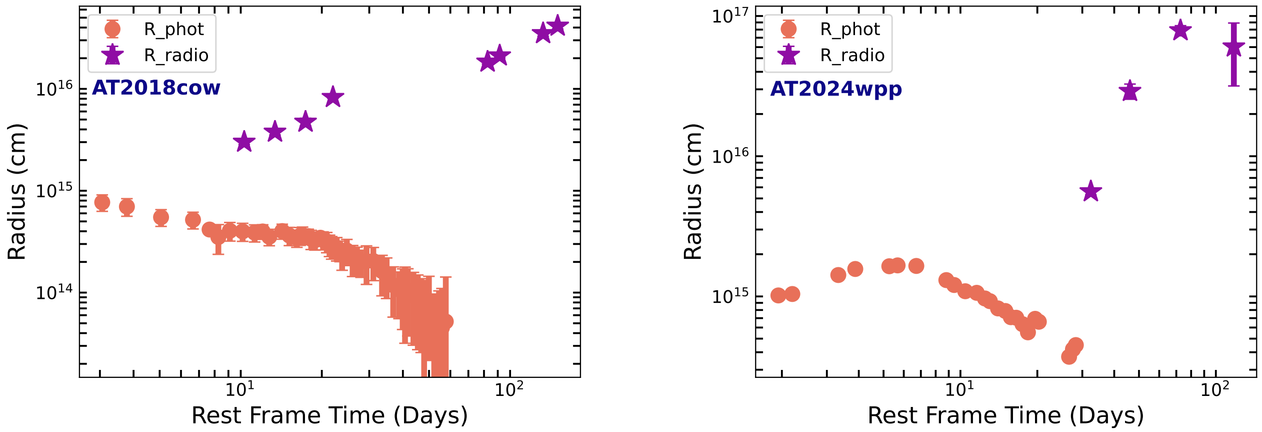

Figure 8. Evolution of the radius of the optical photosphere and radio photosphere of AT 2018cow (left panel; R. Margutti et al. 2019) and AT 2024wpp (right panel; Paper I). The size of the optical photosphere is derived by fitting a blackbody function to the bolometric luminosities. The size of the radio photosphere (rest frame) is estimated by modeling single-epoch radio SEDs adopting the SSA formalism (R. A. Chevalier 1998).

shock velocities, as the IC cooling timescale is a strong function of R and the synchrotron cooling timescale is a strong function of B. It is clear that (not trying to match the absolute numbers) the fluxes at 100 and 200 GHz will decrease from $\delta t \approx 17$ to 32 days in a scenario where fluxes are suppressed owing to cooling, whereas the observed ALMA fluxes are increasing by approximately an order of magnitude. Thus, cooling effects cannot account for the observed sharp rise in millimeter fluxes.

6.2. Off-axis Models

Alternatively, the steep rise of the radio emission can be due to emission from an off-axis relativistic jet, where the emission is initially beamed away from the observer's line of sight. In this scenario, the outflow needs to be a relativistic jet with an initial off-axis viewing angle. The radio emission at early times will be suppressed by relativistic beaming and then increase rapidly as the jet decelerates and relativistic beaming becomes less severe. The millimeter flux density of AT 2024wpp rises approximately an order of magnitude between 17 and 32 days, with a temporal slope of $F_{97.5\,\mathrm{GHz}} \propto t^{4.44 \pm 0.39}$. The temporal indices of synchrotron flux from a nonspreading jet viewed off-axis can be as steep as $F \propto t^{10}$ for a flat CSM density profile (P. Beniamini et al. 2023, see their Table A1). Thus, the observed fast rise in flux densities can be accommodated by off-axis jet models (I. Sfaradi et al. 2025). The millimeter-band flux densities drop to $F_{97.5\,\mathrm{GHz}} \approx 150\,\mu$Jy and $F_{203\,\mathrm{GHz}} \approx 50\,\mu$Jy at $\delta t_{\mathrm{rest}} \approx 46$ days, indicating that the time of peak of the millimeter-band light curve is at $\delta t_{\mathrm{rest}} \approx 32$ days. Note that the abovementioned flux densities at $\delta t_{\mathrm{rest}} \approx 46$ days are from the best-fit SED. After the peak time, the observer should see most of the outflow, and the inferred kinetic energy can be considered to be representative of the actual kinetic energy of the relativistic outflow, implying $E_{k,\mathrm{iso}} \approx 3.3 \times 10^{49}$ erg (from the SED analysis at $\delta t_{\mathrm{rest}} \approx 73$ days). We note that this estimate of $E_{k,\mathrm{iso}}$ is a lower limit owing to the equipartition assumption.

Consider a top-hat jet in which $dE_k/d\Omega = E_{k,\mathrm{iso}}/4\pi$ is constant up to a certain opening angle θ_0 with initial Lorentz factor Γ_0 (where $\Gamma_0 \gg \theta_0^{-1}$) propagating in a medium of the density profile $\rho = \mathrm{A}r^{-k}$. The jet decelerates as it propagates through the medium, and the deceleration radius is given by (P. Beniamini et al. 2023)

$$R_{\mathrm{decl.}} = \left[\frac{(3-k)E_{k,\mathrm{iso}}}{4\pi A c^2 \Gamma_0^2}\right]^{\frac{1}{3-k}} \mathrm{cm}. \tag{12}$$

The corresponding deceleration timescale is $t_{\mathrm{decl.}} = (1+z)R_{\mathrm{decl.}}/2c\Gamma_0^2$ for an on-axis observer. After $t_{\mathrm{decl.}}$, the jet bulk Lorentz factor evolves as $\Gamma(t) \propto t^{-\left[\frac{3-k}{2(4-k)}\right]}$. For an observer located at an angle θ_{obs} from the initial direction of the jet, the peak of the light curve would be at $t_{\mathrm{pk}} = t_{\mathrm{decl.}}(\theta_{\mathrm{obs}}\Gamma_0)^{\frac{8-2k}{3-k}}$. For $E_{k,\mathrm{iso}} \approx 3.3 \times 10^{49}$ erg and $n = 0.3 \times 10^{6}\ \mathrm{cm}^{-3}$ from equipartition analysis (see Table 2), the deceleration radius is $R_{\mathrm{decl.}} \approx 1.2 \times 10^{14}$ cm for $\Gamma_0 = 100$ and $\theta_{\mathrm{obs}} = 30°$. This translates to $t_{\mathrm{pk}} \approx$ 2.3 hr (for $k = 0$) and $t_{\mathrm{pk}} \approx$ 0.07 hr (for $k = 2$), which is significantly smaller than the time of peak of the millimeter emission. This argues against the off-axis jet model for the observed increase in the millimeter emission at $\delta t_{\mathrm{rest}} \approx 17$–32 days. Furthermore, the temporal decay of the millimeter component from $\delta t_{\mathrm{rest}} \approx 32$ days appears to be $F_{97.5\,\mathrm{GHz}} \propto t^{-5.9}$ and $F_{203\,\mathrm{GHz}} \propto t^{-6.8}$ based on the extrapolation to the best-fit SED model at $\delta t_{\mathrm{rest}} \approx 46$ days, which is difficult to explain in an off-axis model. The maximum temporal decay index after jet break is expected to be $F_{\nu} \propto t^{-p}$ (R. Sari et al. 1999). We also note the extremely fast decay of AT 2018cow at ≈230 GHz with a decay index of $F \propto t^{-4.7}$ at $\delta t_{\mathrm{rest}} > 44$ days (see Figure 9), possibly indicating a similar physical origin.

We further explore the off-axis model following the generalized equipartition analysis presented in T. Matsumoto & T. Piran (2023). It is assumed that the observed emission is dominated from a small region of the order π/Γ, where Γ is the bulk Lorentz factor. A critical parameter in this setup is the apparent velocity in Newtonian limits ($\beta_{\mathrm{eq,N}}$) defined by (T. Matsumoto & T. Piran 2023)

$$\beta_{\mathrm{eq,N}} = \frac{(1+z)R_{\mathrm{eq,N}}}{ct}. \tag{13}$$

Here $R_{\mathrm{eq,N}}$ is the Newtonian equipartition radius (listed in Table 2 for AT 2024wpp). $\beta_{\mathrm{eq,N}} = 0.23$ is the critical value above which the relativistic off-axis solution transitions into the Newtonian on-axis branch (T. Matsumoto & T. Piran 2023). Although $\beta_{\mathrm{eq,N}} = 0.23$ was estimated for a maximum viewing angle of π, P. Beniamini et al. (2023) suggest that the critical value is $\beta_{\mathrm{eq,N}} = 0.44$ for a more realistic maximum

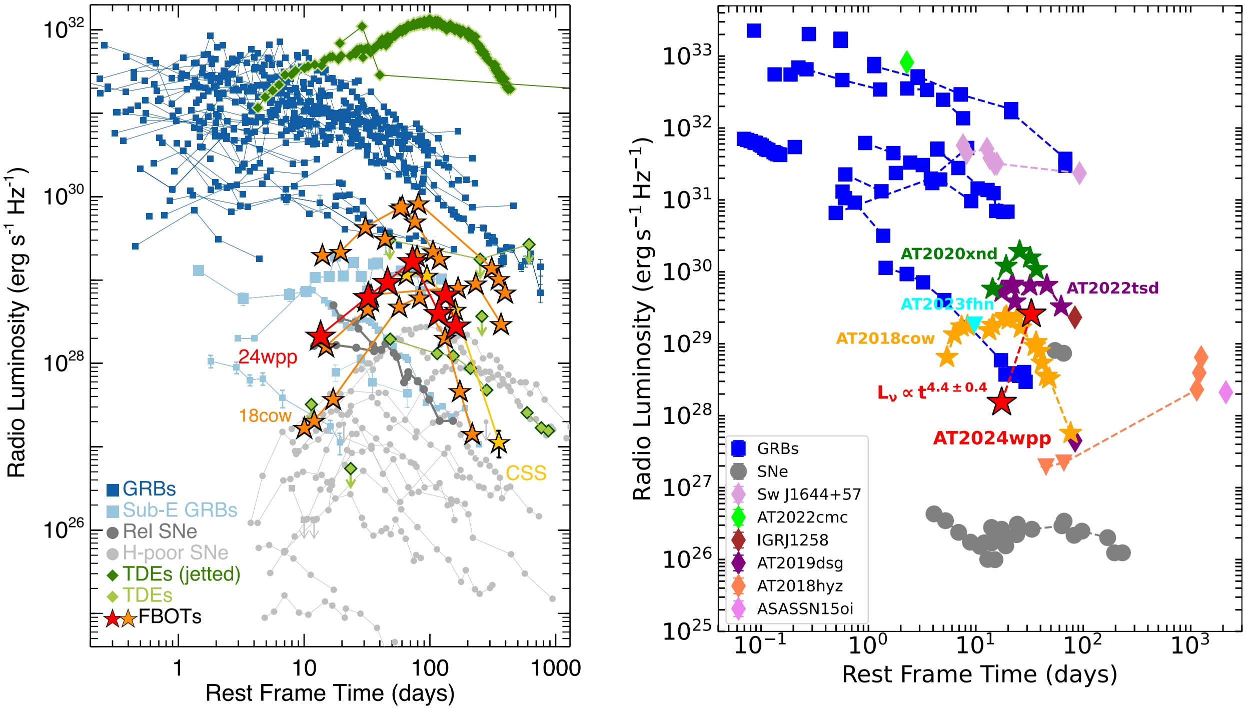

Figure 9. Left panel: radio luminosity light curve of AT 2024wpp at ≈ 10 GHz in the context of other transients. FBOTs stand out for their luminosities that are intermediate between ultrarelativistic GRBs and SNe, while also showing a characteristic bell-shaped light curve peaking at ≈80 days followed by a very steep decay. This shared radio behavior is at the core of the "universal density profile" that we discuss in Section 8.1. Right panel: the (sparsely populated) millimeter-band (80–200 GHz) phase space of light curves of different extragalactic transients GRBs (T. Eftekhari et al. 2022, and references therein), tidal disruption events (E. Berger et al. 2012; Q. Yuan et al. 2016; Y. Cendes et al. 2021; I. Andreoni et al. 2022; D. A. Perley et al. 2022), CCSNe (K. W. Weiler et al. 2007; A. Horesh et al. 2013), and FBOTs (A. Y. Q. Ho et al. 2019, 2022, 2023a, 2023b). In stark contrast with the well-behaved 10 GHz emission, the millimeter emission from even this small sample of FBOTs displays remarkable diversity, likely mirroring the diverse properties of the innermost material the shock emission is emerging from.

viewing angle of $\pi/2$. The apparent velocity for AT 2024wpp appears to increase to $\beta_{\rm eq,N} \approx 0.4$ by $\delta t_{\rm rest} \approx 73$ days (see Table 2), approaching this critical value, and then drops to $\beta_{\rm eq,N} \approx 0.2$ by $\delta t_{\rm rest} \approx 118$ days. The shock energy also increases from $U \approx 0.8 \times 10^{48}$ erg to $\approx 33 \times 10^{48}$ erg during $\delta t_{\rm rest} \approx 32$–73 days. We calculate the radius that minimizes the energy at each epoch for $p = 3$ assuming equipartition ($\epsilon_e = \epsilon_B = 0.33$). We consider four different observer viewing angles $\theta_{\rm obs} = 30°, 45°, 60°, 90°$. At $\delta t_{\rm rest} \approx 118$ days, for an off-axis angle $\theta = 90°$, the model requires $\Gamma \approx 6$ and the corresponding energy is $U \approx 5 \times 10^{49}$ erg. For other viewing angles ($\theta_{\rm obs} = 30°, 45°, 60°$), the inferred velocities at these late times are even higher ($\Gamma > 7$). These high Γ values represent strongly collimated outflows and will not result in emission that peaks at $\delta t_{\rm rest} \approx 32$ days for off-axis observers. Thus, this model does not provide a natural explanation for the observations.

6.3. Radio-emitting Outflow Propagating through a Dense CSM

The SED evolution of AT 2024wpp can be interpreted in a scenario in which the shock interacts with a dense and compact CSM shell at early times ($\delta t_{\rm rest} \approx 17$–32 days). In this case, the radio emission can be initially suppressed by free–free absorption (FFA), and as the shock propagates and emerges out from the dense shell, there is an increase in flux density as a result of the lower optical depth. If the millimeter flux rise is due to the different optical depths, then $F_1/F_2 \propto e^{-\tau_{\rm FFA}} \approx 0.06$, where F_1 and F_2 are the 97.5 GHz flux densities at 17 and 32 days, respectively. We derive $\tau_{\rm FFA} \approx 3$ with $\tau_{\rm FFA} \approx \kappa_{\rm FFA}\, \hat{n}(R_2 - R_1)$. Here $\kappa_{\rm FFA}$ is the free–free opacity and $\hat{n}$ is the average density between an inner R_1 and outer R_2 radius of the dense CSM. The radial extent of this dense medium is also limited, as we observe a steep temporal decay of light curves and an SSA evolution of the SED at $\delta t_{\rm rest} > 32$ days. Assuming the shock emergence to be happening at the edge of the dense shell (D. K. Khatami & D. N. Kasen 2024), we approximate $R_2 \approx 0.56 \times 10^{16}$ cm with the equipartition radius at $\delta t_{\rm rest} \approx 32$ days. We assume the radio-emitting region to be above the optical photosphere (estimated in Paper I) at 17 days, and we use $R_1 \gtrsim 0.06 \times 10^{16}$ cm. The equipartition shock radius at $\delta t_{\rm rest} \approx 17$ days ($\approx 0.05 \times 10^{16}$ cm) is *not* physical, as it does not account for FFA. Free–free opacity ($\kappa_{\rm FFA}$) is defined as (G. B. Rybicki & A. P. Lightman 1979)

$$\kappa_{\rm FFA} = 0.018 \times T_e^{-3/2} Z^2 \hat{n} \nu^{-2} g_{\rm ff}. \tag{14}$$

We infer $\hat{n} \approx 0.5(T/10^5\,{\rm K})^{3/4} \times 10^8 {\rm cm}^{-3}$ assuming constant density between R_1 and R_2. The corresponding CSM mass would be $M_{\rm CSM} \approx 0.07(T/10^5\,{\rm K})^{3/4} M_\odot$. A similar physical scenario was invoked to explain the early bright millimeter emission from AT 2018cow: the size of the CSM shell was inferred to be $\approx 1.7 \times 10^{16}$ cm with a mass $\approx 0.002\, M_\odot$ (A. Y. Q. Ho et al. 2019).

The CSM density profile derived from later ($\delta t_{\rm rest} \approx 46$–118 days) radio SEDs is $\rho_{\rm CSM} \propto r^{-3.10\pm0.16}$ at $R \gtrsim 3 \times 10^{16}$ cm (Figure 10). The shock is expected to accelerate at the outer edge of the dense shell, above which the density profile is steeper than $s > 3$, where $\rho(r) \propto r^{-s}$ (C. D. Matzner & C. F. McKee 1999; E. Waxman & D. Shvarts 1993). The shock velocities derived from the equipartition analysis increase from $\Gamma\beta c = 0.07$ to 0.42 from $\delta t_{\rm rest} \approx 32$ to 73 days, indicating an accelerating shock wave. The shock internal energy increases

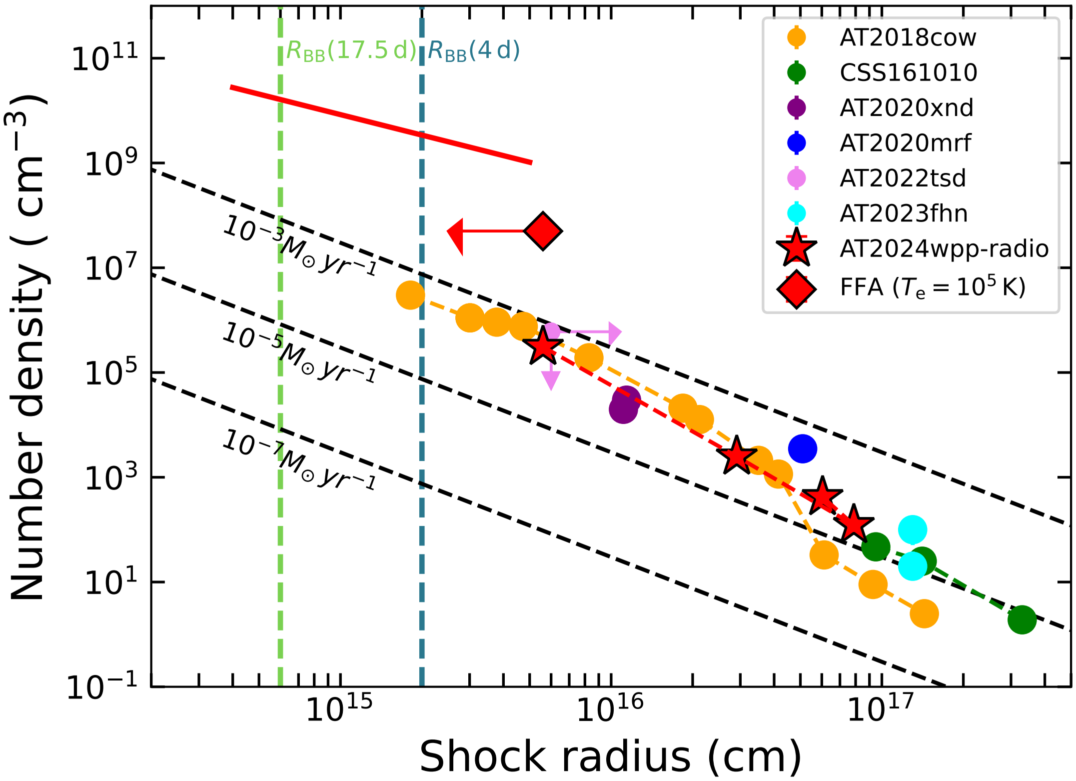

Figure 10. Density profile of the medium around LFBOTs AT 2024wpp (this work), AT 2018cow (A. Y. Q. Ho et al. 2019; R. Margutti et al. 2019), CSS 161010 (D. L. Coppejans et al. 2020), AT2020xnd (J. S. Bright et al. 2022; A. Y. Q. Ho et al. 2022), AT 2020mrf (Y. Yao et al. 2022), AT 2022tsd (A. Y. Q. Ho et al. 2023b), and AT 2023fhn (A. A. Chrimes et al. 2024a). Dashed black lines denote number density profiles corresponding to constant mass-loss rates for an arbitrary wind velocity of $v_w \approx 1000$ km s^{-1}. The vertical blue and green lines denote the position of the optical photosphere at optical peak ($\delta t \approx 4$ days) and at $\delta t \approx 17.5$ days, respectively (Paper I). The solid red line denotes the CSM density profile $\rho_{\rm CSM}(r) \propto r^{-1.3}$ inferred from interpreting the NIR excess as related to effects of free–free emission (see Section 6.2 in Paper I). The inferred CSM density profiles of different events at $>10^{16}$ cm are remarkably similar, which suggests a simple physical mechanism or a self-regulating process (Section 8.1).

from $U \approx 0.8 \times 10^{48}$ erg to $U \approx 33 \times 10^{48}$ erg between these epochs. A high-density medium can efficiently convert the kinetic energy to thermal energy, leading to large radio luminosities (D. K. Khatami & D. N. Kasen 2024). The actual scaling of luminosity would be with the thermal energy per unit radius (U/R). From Equations (7), (4), and (11), one can write $U/R \propto L_{\rm pk}^{8/13}$. Thus, the high millimeter luminosities and SED evolution of AT 2024wpp at early times are consistent with a scenario where the shock is propagating through a dense shell at small radii ($\lesssim 10^{16}$ cm).

In Paper I, we estimate a density profile of $\rho_{\rm CSM}(r) \propto r^{-1.3}$ for the medium above the optical photosphere to account for the NIR excess observed at $\delta t_{\rm rest} \approx 30$ days, under the assumption that the NIR excess is due to free–free optical depth effects in a scattering-dominated medium (see Section 6.2 in Paper I). The optical photosphere is $R_{\rm BB}(30\,{\rm days}) \approx 4 \times 10^{14}$ cm. In this scenario, the observed NIR luminosity implies a density $n \approx 4 \times 10^{8}$ cm^{-3} at $R \approx 10^{16}$ cm. While there are caveats to the NIR excess interpretation, the combined inferences on CSM densities from NIR analysis and radio modeling that we show in Figure 10 paint a picture of a dense shell at $R \lesssim 10^{16}$ cm, with $\rho_{\rm CSM} \propto r^{-3}$ at larger radii.

7. Comparison with Other LFBOTs

7.1. LFBOTs at Radio and Millimeter Wavelengths

Other than AT 2024wpp, there are seven LFBOTs with long-term X-ray and radio observations: AT 2018cow (A. Y. Q. Ho et al. 2019; R. Margutti et al. 2019), CSS 161010 (D. L. Coppejans et al. 2020), AT 2018lug (A. Y. Q. Ho et al. 2020), AT 2020mrf (Y. Yao et al. 2022), AT 2020xnd (J. S. Bright et al. 2022; A. Y. Q. Ho et al. 2022) AT 2022tsd (A. Y. Q. Ho et al. 2023b), and AT 2023fhn (A. A. Chrimes et al. 2024a). Out of these seven, only three are detected in the millimeter bands: AT 2018cow (A. Y. Q. Ho et al. 2019), AT 2020xnd (J. S. Bright et al. 2022; A. Y. Q. Ho et al. 2022), and AT 2022tsd (A. Y. Q. Ho et al. 2023b; D. Matthews et al. 2023). In Figure 9, we show the 8–10 GHz light curves of all detected LFBOTs, along with other transients, and a compilation of light curves of all millimeter transients with the four millimeter-bright LFBOTs.

One of the most striking features is the similarity in rise timescales and the rapid flux decay across all radio-bright FBOTs in the radio bands, as highlighted in the left panel of Figure 9. This is also reflected in Figure 11, where FBOTs occupy a distinct and compact region of the parameter space. Instead, the millimeter emission from even a very small sample of LFBOTs shows an impressive range of behaviors and luminosities (e.g., there is a factor >100 difference between the millimeter luminosity of AT 2022tsd and that of AT 2024wpp at ≈20 days). This phenomenology likely primarily reflects the diversity of the innermost medium around LFBOTs versus the more "universal" CSM at $>10^{16}$ cm, in addition to possible differences in their central engines.

Broadly speaking, the properties of the radio emission from AT 2024wpp are in line with those of other LFBOTs.

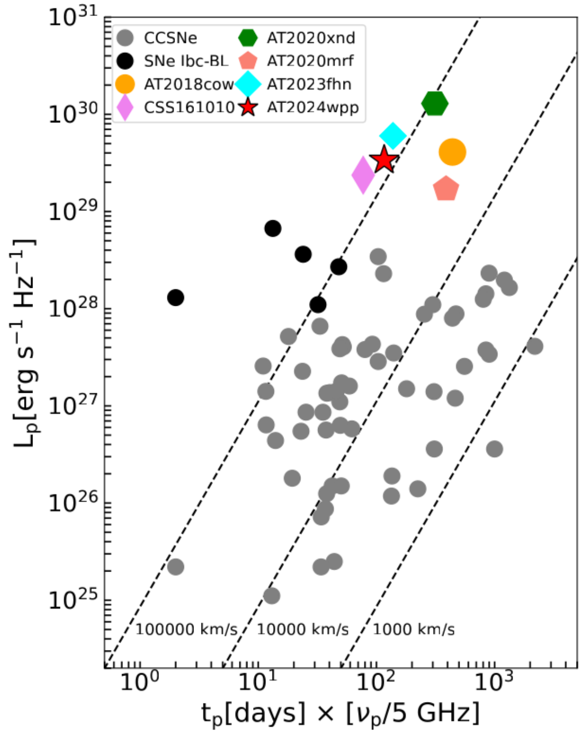

Figure 11. Radio spectral luminosities of different astrophysical transients. L_p denotes the peak spectral luminosity in the 8–10 GHz band. ν_p and t_p represent the peak frequency and peak time of the radio SED, respectively. The dashed lines denote the mean shock velocity in an SSA scenario (R. A. Chevalier 1998). References: R. Margutti et al. (2019), A. Y. Q. Ho et al. (2019), D. L. Coppejans et al. (2020), J. S. Bright et al. (2022), A. Y. Q. Ho et al. (2022), Y. Yao et al. (2022), A. A. Chrimes et al. (2024a).

Specifically, AT 2024wpp shows the steep rise and very steep decay that are hallmark observational features of LFBOTs compared to other transients at centimeter wavelengths (Figure 9, left panel). The peak radio spectral luminosity of AT 2024wpp is $L_{9\mathrm{GHz}} \approx 1.7 \times 10^{29}$ erg s^{-1} Hz^{-1} at $\delta t \approx 73$ days, similar to that of other LFBOTs (see Figure 9, left panel) with a steep post-peak temporal decay index of $F_{9\,\mathrm{GHz}} \propto t^{-2.05\pm0.54}$.

However, the SED evolution of AT 2024wpp is unique and distinct compared to that of other LFBOTs (i) at early times $\delta t_{\mathrm{rest}} < 32$ days and (ii) at $\delta t_{\mathrm{rest}} \approx 133$ days, when we observe a spectral radio inversion. The evolution of millimeter-band flux densities during $\delta t_{\mathrm{rest}} \approx 17 - 32$ days is unprecedented, with $\nu_{\mathrm{pk}} \propto t^{-2.01\pm0.65}$ and $F_{\mathrm{pk}} \propto t^{4.04\pm0.42}$. The closest analog is AT 2018cow, though the millimeter rise is not as extreme (Figure 9, right panel). In both events, the rapid millimeter brightening can be attributed to the shock propagating through a dense and radially confined medium and efficiently converting the ejecta kinetic energy into thermal energy (A. Y. Q. Ho et al. 2019; D. K. Khatami & D. N. Kasen 2024).

The average blast wave velocity of AT 2024wpp increases from $\Gamma\beta c \approx 0.07c$ to $0.42c$ between $\delta t_{\mathrm{rest}} \approx 32$ and 73 days and then decreases to $0.2c$ by $\delta t_{\mathrm{rest}} \approx 118$ days. This acceleration is consistent with the shock breaking out of the dense CSM shell and entering a lower-density medium. While not as evident as in AT 2024wpp, AT 2018cow also shows indication of an accelerating blast wave with velocities going from $v \approx 0.1c$ at early times ($\delta t \approx 22$ days; A. Y. Q. Ho et al. 2019) to $v \approx 0.2c$ at later times (see Figure 13 of R. Margutti et al. 2019; A. J. Nayana & P. Chandra 2021). Radio spectral information on AT 2018lug is limited; CSS 161010 shows evidence for a decelerating outflow between $\delta t \approx 69$ and 357 days and does not have observations at early times.

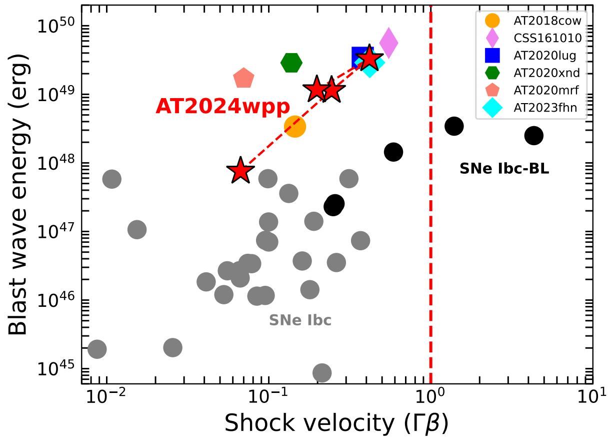

Figure 12. Blast wave energy vs. shock velocity of FBOTs AT 2024wpp ($\delta t \approx 32$–118 days), AT 2018cow ($\delta t \approx 22$ days), CSS 161010 ($\delta t \approx 99$ days), AT 2020xnd ($\delta t \approx 38$ days), AT2022mrf ($\delta t \approx 261$ days), and AT 2023fhn ($\delta t \approx 138$ days). References: R. Margutti et al. (2019), A. Y. Q. Ho et al. (2019), D. L. Coppejans et al. (2020), J. S. Bright et al. (2022), A. Y. Q. Ho et al. (2022), Y. Yao et al. (2022), A. A. Chrimes et al. (2024a).

For AT 2024wpp, the SEDs evolve as $\nu_{\mathrm{pk}} \propto t^{-2.99\pm0.10}$ and $F_{\mathrm{pk}} \propto t^{-0.67\pm0.06}$ during $\delta t_{\mathrm{rest}} \approx 32$–73 days. At later times ($\delta t_{\mathrm{rest}} > 118$ days), the SED evolution is characterized by $\nu_{\mathrm{pk}} \propto t^{-0.60\pm1.05}$ and $F_{\mathrm{pk}} \propto t^{-2.05\pm0.54}$. In the case of AT 2018cow, the SED evolution at $\delta t > 80$ days followed $\nu_{\mathrm{pk}} \propto t^{-2.2\pm0.1}$ and $F_{\mathrm{pk}} \propto t^{-1.7\pm0.1}$ (A. Y. Q. Ho et al. 2019; R. Margutti et al. 2019). CSS 161010 showed an evolution of $\nu_{\mathrm{pk}} \propto t^{-1.26\pm0.07}$ and $F_{\mathrm{pk}} \propto t^{-1.79\pm0.09}$ at $\delta t > 99$ days (D. L. Coppejans et al. 2020). In terms of $\nu_{\mathrm{pk}}(t)$ and $F_{\mathrm{pk}}(t)$, the SED evolution of AT 2024wpp at $\delta t \gtrsim 32$ days closely resembles that of other radio-bright FBOTs. The spectral peak frequency (ν_{pk}) cascading to lower values over time is broadly consistent with expectations of an expanding shock wave. However, the $\nu_{\mathrm{pk}}(t)$ and $F_{\mathrm{pk}}(t)$ of LFBOTs are significantly different from those seen in typical CCSNe interacting with a wind-like CSM (where we expect $\nu_{\mathrm{pk}} \propto t^{-1}$ and $F_{\mathrm{pk}} \sim$ constant). The relatively faster evolution of ν_{pk} and F_{pk} seen in LFBOTs is indicative of a steeper CSM density profile than that of a canonical wind-like profile ($\rho_{\mathrm{CSM}}(r) \propto r^{-2}$).

LFBOTs are also clearly distinct from ordinary CCSNe in terms of shock velocity. We plot AT 2024wpp, along with other LFBOTs and SNe, in the velocity-energy phase space in Figure 12. AT 2024wpp has an inferred outflow velocity of $\Gamma\beta c \approx 0.4c$ at $\delta t \approx 73$ days and belongs to the class of LFBOTs that show mildly relativistic outflows similar to CSS 161010 (D. L. Coppejans et al. 2020), AT 2018lug (A. Y. Q. Ho et al. 2020), and AT 2023fhn (A. A. Chrimes et al. 2024a). The outflow velocity of AT 2018lug is $\Gamma\beta c \geqslant 0.3c$ at $\delta t \approx 100$ days, and that of CSS 161010 is $\Gamma\beta c \geqslant 0.55c$ at a similar epoch. These outflow velocities are higher compared to the non-relativistic velocities seen in AT 2018cow ($v \sim 0.1c$; A. Y. Q. Ho et al. 2019; R. Margutti et al. 2019). At $\delta t \approx 73$ days, the kinetic energy coupled to the fast-moving radio-emitting shock of velocity $\Gamma\beta \approx 0.4c$ is $E_k \approx 3.3 \times 10^{49}$ erg. For a standard spherical hydrodynamical collapse of a star, this would imply $E_k > 10^{55}$ erg coupled with the slow-moving material at $v \approx 10{,}000$ km s^{-1}, where $E_k \propto (\Gamma\beta)^{-5.2}$ for a polytropic index of 3 (J. C. Tan et al. 2001). This energy

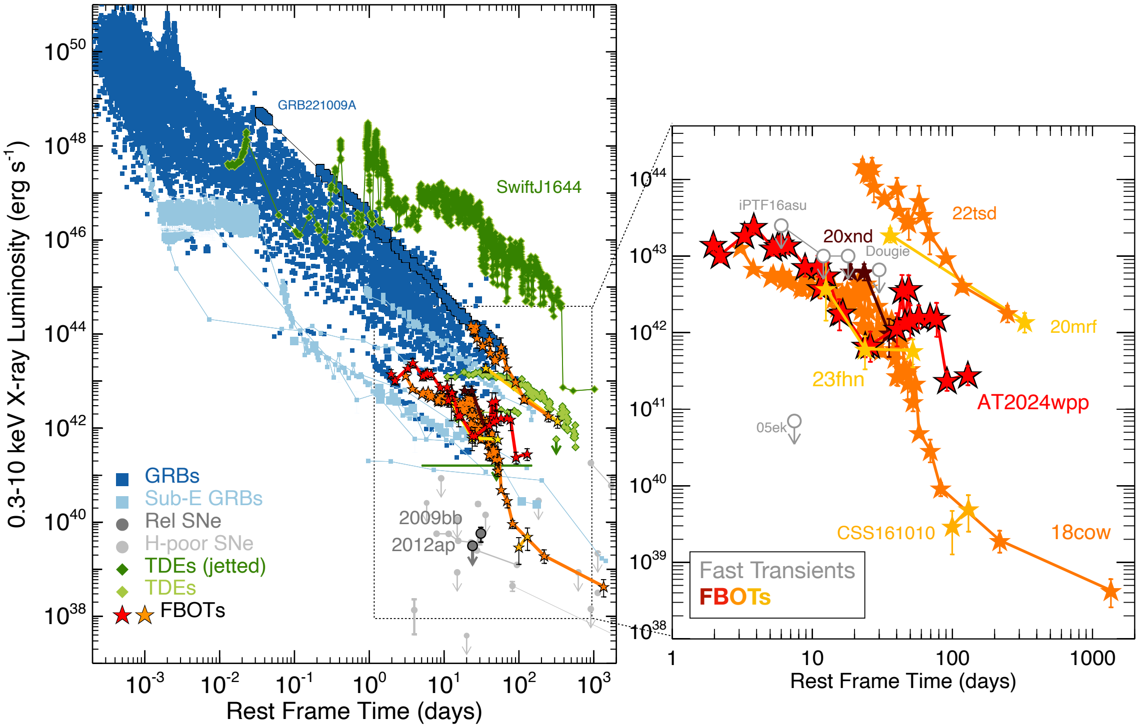

Figure 13. Left panel: soft X-ray luminosity evolution of AT 2024wpp in the context of explosive transients capable of launching relativistic ejecta (long GRBs, tidal disruption events, H-poor SNe). FBOTs span the entire dynamical range of X-ray luminosity observed for long GRBs to date. Right panel: zoom-in of the region of luminous FBOTs with X-ray emission (stars) and fast transients (open gray circles). AT 2024wpp is only the second FBOT for which we were able to sample the X-ray emission at $\delta t < 10$ days. While the initial $L_x \approx$ a few $\times\ 10^{43}$ erg s^{-1} is not dissimilar from AT 2018cow, AT 2020xnd, and AT 2023fhn, AT 2024wpp stands out at later times $\delta t \gtrsim 30$ days for its longer-lived and spectrally harder X-ray emission. Similar to AT 2018cow is the remarkably fast late-time decay. We add to this panel other fast transients observed in the X-rays: of these, the very luminous and fast-evolving optical emission from "Dougie" bears close similarities to luminous FBOTs. References: R. Margutti et al. (2013, 2019), D. L. Coppejans et al. (2020), J. S. Bright et al. (2022), Y. Yao et al. (2022), D. Matthews et al. (2023), A. Y. Q. Ho et al. (2023b), A. A. Chrimes et al. (2024b), G. Migliori et al. (2024) and references therein.

largely exceeds the limit ($E_k \approx 10^{51}$ erg) of typical neutrino-driven stellar explosions (challenging most stellar explosion models) and argues against a spherical stellar collapse as the astrophysical origin of AT 2024wpp.

Finally, a unique radio aspect of AT 2024wpp is the evidence for radio spectral inversion at $\delta t_{\rm rest} \approx 133$ and 161 days (see Figure 7). The spectral behavior indicates that $\nu_{\rm pk} \gtrsim 9$ GHz, implying $R < 6 \times 10^{16}$ cm at these epochs, which is smaller than the shock radius at $\delta t_{\rm rest} \approx 118$ days. This could be indicative of another outflow, possibly associated with slow disk winds and/or due to a complex CSM density profile.

To summarize, even though the sample is limited, LFBOTs present a combination of radio properties that make them clearly distinct from other transients (like the rapid rise and decay of their radio light curves), while at the same time showing significant diversity in terms of spectral evolution and outflow velocities. The properties of AT 2024wpp are particularly striking owing to the accelerating outflow with increasing shock internal energy. We present a detailed comparison of the inferred CSM densities of LFBOTs and their astrophysical implication in Section 8.1.

7.2. LFBOTs in the X-Rays

Only LFBOTs have been detected in the X-rays (Figure 13), showing very luminous displays $L_x > 10^{43}$ erg s^{-1} in line with those of long GRBs: the FBOT AT 2022tsd (A. Y. Q. Ho et al. 2023b; D. Matthews et al. 2023) even rivals GRB 221009A, the brightest GRB detected so far. We note that our independent spectral extraction and reanalysis of the FBOT AT 2023fhn do not confirm the claim of subluminous X-ray emission by A. A. Chrimes et al. (2024b) and point instead to a harder spectrum (and hence more luminous emission) than what was assumed by those authors, in line with other FBOTs. While LFBOTs share with GRBs[49] rapid X-ray variability timescales ($\Delta t/t < 1$) and the nonthermal nature of their X-ray emission, their spectral properties are markedly different: GRB X-ray afterglow emission is typically consistent with an $F_\nu \propto \nu^{-1}$ spectrum (e.g., R. Margutti et al. 2013), while LFBOTs have harder spectra even before the emergence of the Compton hump for years after the FBOT (G. Migliori et al. 2024).

Among FBOTs, only AT 2024wpp and AT 2018cow have shown clear evidence for a Compton hump of emission. However, it is interesting to note that the hard 0.3–10 keV spectrum $F_\nu \propto \nu^0$ of the very X-ray-luminous AT 2020mrf at $\approx$330 days, compared to its significantly softer spectrum $F_\nu \propto \nu^{-0.8}$ at early times $\approx$36 days (Y. Yao et al. 2022), is suggestive of similar phenomenology and evolution to those in AT 2024wpp and AT 2018cow, albeit on a significantly longer timescale. At the time of writing there are only seven other LFBOTs with published X-ray light curves: at $\delta t \approx 20$ days, when most of the sample has observations, the sample covers a $\approx 10^2$ dynamic range of luminosities with two groups of LFBOTs: "18cow-like" FBOTs with a plateau+steep decay

---

[49] Tidal disruption events are also known to show rapid X-ray variability, while no known SN displayed rapid soft X-ray variability weeks after explosion (see, e.g., V. V. Dwarkadas 2025, for a recent review). Rapid X-ray variability is a hallmark feature of engine-driven transients.

light-curve morphology, and "22tsd-like" FBOTs displaying the most luminous X-ray emission. Given the likely geometrically beamed nature of the emission (Section 4.3), we consider it possible that the observed diversity is in part due to viewing angle effects, with pole-on views being associated with more luminous displays.

8. Plausible Physical Models

Various progenitor models have been proposed to explain the observed properties of FBOTs. Here we explore different physical models that could explain the X-ray and radio properties of AT 2024wpp. Based on the observations presented in this work, the progenitor system of AT 2024wpp should be able to produce (1) luminous and variable X-ray emission with a nonthermal spectrum and a transient Compton hump appearing at $\delta t \approx 50$ days, (2) a shock carrying $E_k \approx 3.3 \times 10^{49}$ erg with velocities as fast as $v \approx 0.4c$ at $\delta t_{\rm rest} \approx 73$ days, (3) a dense CSM of $n \approx 0.3 \times 10^6\,{\rm cm}^{-3}$ at a distance of $R \approx 0.6 \times 10^{16}$ cm from the explosion center and significantly larger densities inward, and (4) a radial density profile of $\rho_{\rm CSM} \propto r^{-3.1}$ extending up to $R \approx 10^{17}$ cm.

Progenitor models that exclusively rely on CSM interaction (O. D. Fox & N. Smith 2019; S.-C. Leung et al. 2021; C. Pellegrino et al. 2022) cannot explain the presence of variable, nonthermal X-ray emission and do not provide a natural explanation for the mildly relativistic outflows that characterize LFBOTs; hence, CSM-interaction-only models can be ruled out. The relativistic outflows imply the presence of compact objects. Indeed, a class of viable LFBOT models involves the presence of a central engine: a failed SN that produces an accreting BH and small ejecta mass ejected via accretion disk winds (E. Quataert et al. 2019; A. Antoni & E. Quataert 2022), a successful CCSN from a rotating massive star that gives birth to a BH or NS (R. Margutti et al. 2019; D. A. Perley et al. 2019; O. Gottlieb et al. 2022), pulsational pair instability SNe (S.-C. Leung et al. 2020), tidal disruption of a star by an intermediate-mass BH or stellar-mass BH (N. P. M. Kuin et al. 2019; D. A. Perley et al. 2019; K. Kremer et al. 2021; C. P. Gutiérrez et al. 2024), merger-induced tidal disruption and hyperaccretion of a W-R star by an NS or BH (B. D. Metzger 2022), and collision of a newly born NS or BH from a core-collapse explosion with a companion star, leading to tidal disruption and hyperaccretion (D. Tsuna & W. Lu 2025). Although these models can drive nonrelativistic to mildly relativistic outflows, since they invoke an accretion disk around a BH/NS in some regime of hyperaccretion (A. Sadowski & R. Narayan 2015, 2016), reproducing the quasi-universal density profile of Figure 10 is more challenging. We expand on this aspect in the next section.

8.1. A Universal CSM Density Profile in LFBOTs

The density profile of the environment of AT 2024wpp is $\rho_{\rm CSM}(r) \propto r^{-3.10 \pm 0.16}$, shown in Figure 10 at $R \gtrsim 6 \times 10^{15}$ cm, along with that of other LFBOTs. The environmental densities of LFBOTs are strikingly similar, with $n \approx 10^6\,{\rm cm}^{-3}$ at $R \approx 10^{16}$ cm and an approximate profile $\rho_{\rm CSM} \propto r^{-3}$ at distances ≈ a few times 10^{15}–10^{17} cm. The innermost density profile at $<3 \times 10^{15}$ cm has only been sampled with radio observations for AT 2018cow (A. Y. Q. Ho et al. 2019; R. Margutti et al. 2019) and AT 2024wpp. In both cases, there is some evidence for a flatter inner density profile (see the first four points in orange in Figure 10 for AT 2018cow). For AT 2024wpp the evidence comes from two angles: first, the rapid millimeter-band rise of Section 6.3; second, the NIR excess observed at $\delta t \approx 30$ days being consistent with free–free opacity effects occurring in an extended medium of a shallow density profile of $\rho \propto r^{-1.3}$ above the optical photosphere at $R_{\rm BB} \approx 4 \times 10^{14}$ cm (see Section 6.2 of Paper I).

Based on these observations, we find that the LFBOT environment likely consists of a high-density component with a flat profile up to distances of a few times 10^{15}–10^{16} cm and a steep density profile $\rho_{\rm CSM} \propto r^{-3}$ outward. These broadly similar LFBOT CSM density profiles are likely manifestations of similar stellar evolution processes. We discuss the astrophysical implications below.

While clearly not consistent with wind-like density profiles $\rho \propto r^{-2}$ (which are the result of constant mass-loss-to-wind-velocity ratio), the environmental densities of LFBOTs correspond to *effective* mass-loss rates up to $\dot{M} \approx 10^{-3}\,M_\odot\,{\rm yr}^{-1}$ for an arbitrary wind velocity of $v_w = 1000\,{\rm km\,s}^{-1}$ (Figure 10). These effective $\dot{M}$ are significantly higher than those of H-stripped CCSNe (e.g., R. A. Chevalier et al. 2006) and long GRBs (e.g., B. P. Gompertz et al. 2018).[50] Such dense environments can be formed during the brief evolutionary phases of intense mass loss from some massive stars (N. Smith 2014). However, the presence of dense material at such close distances from the LFBOTs requires some form of timing between the mass ejection event (s) and the onset of the LFBOT emission. Some LFBOT models struggle to provide a natural explanation for this timing (and hence explain the quasi-universal CSM density profile of LFBOTs at $\gtrsim 10^{16}$ cm). Among these is the pulsation pair instability (PPI) SN model (S. E. Woosley 2017), for which the CSM density is set by previous PPI events (M. Renzo et al. 2020; S.-C. Leung et al. 2021). Even for (single-star) models that involve the presence of a BH/NS and can in principle create large densities at $R \lesssim 10^{16}$ cm (like the failed explosion of a single massive star ejecting a small amount of ejecta via disk winds, or the successful core collapse of a massive star-forming NS or BH), some fine-tuning is required between the mass loss and progenitor's evolutionary phase to reproduce observations.

More natural explanations of the universal CSM density profile observed in LFBOTs are offered by models like (i) a merger-initiated tidal disruption and hyperaccretion of a W-R star onto an NS or BH binary companion (B. D. Metzger 2022) and (ii) the collision of a newly born NS or BH from a core-collapse explosion with a companion star (D. Tsuna & W. Lu 2025). The appeal of these models is that they can reproduce other key observational LFBOT properties like the asymmetric ejecta, variable nonthermal X-ray emission (potentially with a Compton hump), and mildly relativistic outflow velocities (this is fundamentally because both models involve super-Eddington accretion on a compact object).

In the first model (i) by B. D. Metzger (2022), dense and confined CSM is established by the premerger W-R star mass loss (O. Pejcha et al. 2016b, 2016a, 2017; M. MacLeod et al. 2017; M. MacLeod & A. Loeb 2020) on radial scales $\approx 10^{14}$–10^{15} cm (T. Matsumoto & B. D. Metzger 2022), which will be similar in all W-R star/BH–NS mergers. The extended CSM ($R \gtrsim 10^{15}$ cm) results from circumbinary disk outflows

---

[50] We limit our comparison to H-poor stellar explosions, as the LFBOT ejecta is H depleted (see Paper I).

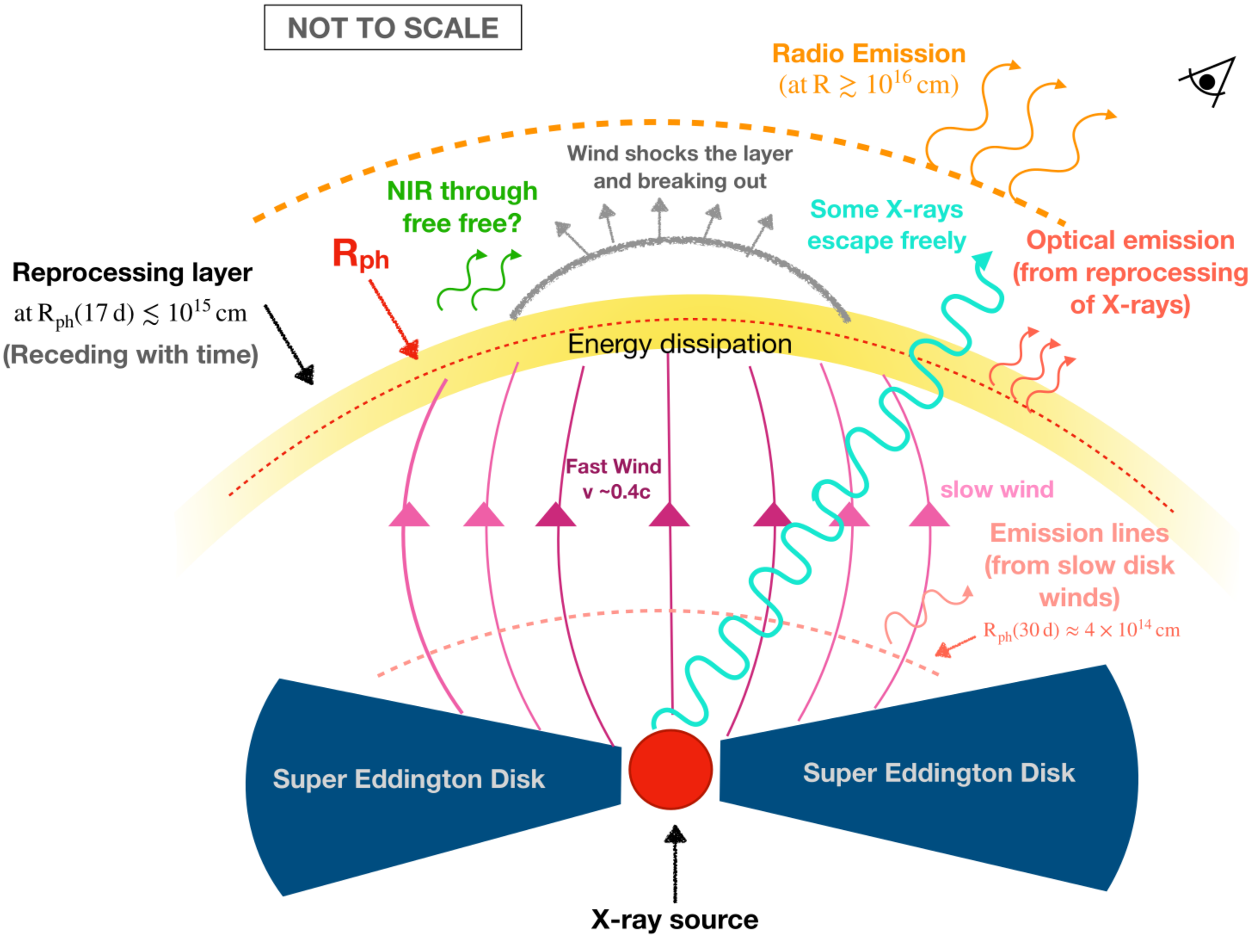

Figure 14. A cartoon diagram (not to scale) showing the geometry of AT 2024wpp and various emission components in the context of an engine-driven progenitor model. The physical picture is motivated by the models presented in D. Tsuna & W. Lu (2025) and B. D. Metzger (2022). Both these models invoke super-Eddington accretion onto a compact object (NS or BH) in different astrophysical contexts. The disk wind outflows from the accretion disk generate ^{56}Ni-poor asymmetric ejecta with a range of velocities—fast outflow ($v \approx 0.4c$) from the interior of the accretion disk and slow winds from the outer radii of the disk. In this framework, the X-ray emission originates from the central engine, while the optical emission arises from reprocessing of X-rays. Here we are agnostic about the reprocessing layer, whereas D. Tsuna & W. Lu (2025) assume it to be an SN ejecta and B. D. Metzger (2022) assumes it to be the fast disk wind ejecta. The low-velocity emission lines are from the slow disk winds from the outer radii of the accretion disk. Radio emission arises owing to the interaction between fastest disk wind and CSM at $R \gtrsim 10^{16}$ cm.

(D. Hollenbach et al. 1994; E. Keto 2007) and the circumbinary relic disk from the common envelope phase (A. Kashi & N. Soker 2011). The properties of this extended CSM can depend on the binary parameters and mass transfer. Probing the extended CSM of LFBOTs at radial scales $R \gg 10^{18}$ cm in the future might help reveal their diversity in this regard. In the model proposed by D. Tsuna & W. Lu (2025), the observational characteristics of FBOTs are best reproduced in a scenario where the accreting NS/BH is formed from the explosion of a low-mass ($\lesssim 3\ M_\odot$) helium star. Mass transfer at a rate of $\approx 10^{-4}\,M_\odot\,\mathrm{yr}^{-1}$ onto the companion can occur from the helium star at 0.1−1 kyr before the core collapse (T. M. Tauris et al. 2015; S. C. Wu & J. Fuller 2022; A. Ercolino et al. 2025). For typical equatorial mass-loss speeds (10–100 km s^{-1}) from the binary, this translates to distances $R \gtrsim 10^{15}$–10^{17} cm. In the decades before the explosion, extreme mass-loss rates $\gtrsim 10^{-2}\,M_\odot\,\mathrm{yr}^{-1}$ can occur as a result of the rapid expansion of the outer layer of the helium star (S. C. Wu & J. Fuller 2022). This will lead to dense CSM at radius $R \lesssim 10^{15}$ cm.

To conclude this section, at the time of writing, the most promising LFBOTs models are those that involve binary systems, where outflows launched by a hyperaccreting compact object interact with an environment that was shaped by the previous evolution of the binary.

8.2. The Geometry of AT 2024wpp and Various Emission Components

Figure 14 represents a schematic illustration (not to scale) of the geometry of AT 2024wpp and various emission components in the context of a progenitor model involving a central engine. This physical picture is motivated by the models presented in B. D. Metzger (2022) and D. Tsuna & W. Lu (2025). While these models are different in their astrophysical context, both of them invoke super-Eddington accretion onto a compact object (NS or BH). The disk wind outflows powered by the release of gravitational energy (R. Narayan & I. Yi 1995; R. D. Blandford & M. C. Begelman 1999; T. Kitaki et al. 2021) generate the ^{56}Ni-poor aspherical ejecta in a velocity range observed in FBOTs. The outflow speed of disk winds from the outer radii of the accretion disk is low, with mean velocities $\approx$3000–4000 km s^{-1} (B. Margalit & B. D. Metzger 2016; B. D. Metzger 2022), which can explain the low-velocity emission lines seen in AT 2024wpp (Paper I). The disk wind outflow velocities from the interior part of the accretion disk are much higher; results from GRMHD simulations of super-Eddington accretion disks indicate transrelativistic outflow velocities (A. Sadowski & R. Narayan 2015, 2016).

X-ray emission is from the central engine. Depending on the viewing angle and X-ray covering fraction, some X-rays can escape early on and be detected. X-ray emission from AT 2024wpp is detected from $\delta t \approx 2$ days. The transient Compton hump seen in the X-rays naturally fits in this scenario, as the X-ray source is embedded in an expanding ejecta with time-variable optical depth to Compton scattering. Optical emission is powered by the reprocessing of X-ray emission, where the origin and nature of the reprocessing layer are different in these two models. In the D. Tsuna & W. Lu (2025) model, the collision between a newly born NS/BH and the companion star leads to tidal disruption and super-Eddington accretion. The fast disk winds collide with the SN ejecta, effectively converting wind kinetic energy to radiation, resulting in a luminous optical transient with peak luminosity $L_{\rm pk} \approx 10^{44}$ erg s^{-1}. In the B. D. Metzger (2022) model, a W-R star in a binary system is tidally disrupted and accreted onto the NS/BH. The optical emission is due to a combination of reprocessing of X-rays from the inner accretion disk/jets by fast disk wind ejecta and shock interaction between the disk wind outflow and premerger CSM of the W-R star. Based on our multiwavelength observations and analysis of AT 2024wpp (Paper I; this work), we remain agnostic about the origin and nature of the reprocessing layer and hypothesize that the optical radiation is reprocessed X-rays from the central engine. From the NIR analysis, the mass of the reprocessing layer is $M \approx 2\ M_\odot$ (Paper I) and is likely to be preexisting material. However, we emphasize that the preexisting material need not be the only medium that reprocesses the X-rays, as the fast disk winds could also contribute to the process (B. D. Metzger 2022). In any case, it is less likely that the reprocessing layer is SN ejecta, as SN Ib/c ejecta would develop some CNO lines in the optical spectra at later times, which we do not see in the case of AT 2024wpp, unless the nondetection is due to the low CNO mass fraction in low-mass helium stars (L. Dessart et al. 2020, 2021). Radio emission arises as a result of shock interaction between the fastest disk wind outflow and the CSM at $r \approx 10^{16}$–10^{18} cm. The blast wave velocities inferred from radio SED modeling of AT 2024wpp go up to $\Gamma\beta c \approx 0.42c$, in line with the prediction of mildly relativistic disk wind outflows from super-Eddington disks from simulations (A. Sadowski & R. Narayan 2015, 2016). This physical picture is consistent with the results presented in M. Pursiainen et al. (2025), as at early times the optical photosphere is inside the fast-moving outflow.

The high disk wind velocities can be used to put rough constraints on the mass and size of the central compact source. For the typical mass ($M \approx 1.1\ M_\odot$) and size ($R \approx 12$ km) of an NS, the escape velocity will be $v_{\rm esc} \approx 0.5c$. Thus, the observed outflow velocities can be barely achieved in the disk winds from an NS, whereas they can be easily achieved from a BH (A. Sadowski & R. Narayan 2015, 2016). Radiation hydrodynamic simulations of supercritical accretion onto an NS predicts outflow velocities $v \approx 0.2c$–$0.3c$ (K. Ohsuga 2007), while GRMHD simulations predict velocities $v \approx 0.4c$ (H. R. Takahashi & K. Ohsuga 2017). The large energy budget of AT 2024wpp ($E_{\rm rad} = 10^{51}$ erg from Paper I) also favors a BH over an NS (see Section 2.4 of D. Tsuna & W. Lu 2025).

9. Summary and Conclusions

We present extensive X-ray (0.3–79 keV) and radio (0.25–203 GHz) observations of the FBOT AT 2024wpp spanning $\delta t \approx 2$–280 days after first light. Major findings from the combined X-ray and radio analysis are the following:

1. AT 2024wpp shows luminous and variable X-ray emission, being only the third FBOT with a hard X-ray detection. The X-ray luminosity ($L_{\rm x} \approx 1.5 \times 10^{43}$ erg s^{-1}) remains roughly constant in the first 7 days and then decays with an index of $L_{\rm x} \propto t^{-2.5 \pm 0.25}$, followed by a rebrightening (flaring) that starts at $\delta t \approx 35$ days and peaks at $\delta t \approx 50$ days (see Figure 1).
2. The X-ray spectra are initially soft ($F_\nu \propto \nu^{-0.8}$) and gradually transition to a harder state over time with an extremely hard spectrum ($F_\nu \propto \nu^{1.25}$) at the peak of the rebrightening ($\delta t \approx 50$ days). The spectrum becomes soft ($F_\nu \propto \nu^{-0.6}$) again at $\delta t \approx 75$ days after the flare peak (Figures 1, 3, and 4).
3. The X-ray emission from AT 2024wpp shows clear evidence for a transient Compton hump at $\delta t \gtrsim 50$ days, similar to that of AT 2018cow, in which the Compton hump was present at much earlier times ($\delta t \approx 8$ days). Compton humps are unprecedented in the field of stellar explosions but are commonly observed in accretion-powered systems like AGNs and XRBs.
4. The spectral and temporal evolution of X-ray emission from AT 2024wpp favors the presence of a high-energy source embedded inside expanding aspherical ejecta, similar to the picture invoked to explain AT 2018cow (R. Margutti et al. 2019). The delayed appearance of the Compton hump in AT 2024wpp relative to AT 2018cow can be attributed to a variety of effects, including time-dependent ionization of the ejecta and larger ejecta mass.
5. AT 2024wpp displays luminous radio emission with a peak spectral luminosity of $L_{\rm 9GHz} \approx 1.7 \times 10^{29}$ erg s^{-1} Hz^{-1} at $\delta t_{\rm rest} \approx 73$ days, significantly larger than SNe and comparable to other LFBOTs (see Figure 9). Radio emission is also detected in the millimeter bands (97.5 and 203 GHz) at $\delta t_{\rm rest} \approx 17$ and 32 days, marking AT 2024wpp as the fourth millimeter-bright FBOT.
6. The radio spectral evolution is unprecedented, with an extremely rapid rise in the millimeter flux densities at early times $\delta t_{\rm rest} \approx 17$–32 days. Subsequently, the spectral peak flux slowly declines with peak frequency cascading to lower bands as expected in a shock-driven synchrotron emission model. At a later time ($\delta t_{\rm rest} > 118$ days), we find first evidence for a spectral inversion, possibly indicating the emergence of a new emission component (see Figure 7).
7. The shock velocities from radio SED modeling indicate an accelerating outflow with velocities evolving from $\Gamma\beta c \approx 0.07c$ to $0.42c$ during $\delta t_{\rm rest} \approx 32$–73 days with an increasing amount of energy ($U \approx 0.8$–33×10^{48} erg) coupled to this outflow (see Table 2).

8. We interpret the radio emission from AT 2024wpp in a scenario in which the radio-emitting shock is propagating through a dense CSM shell of outer radius $\approx 10^{16}$ cm. The shock then accelerates at the edge of this shell through a medium of the density profile $\rho_{\rm CSM}(r) \propto r^{-3}$ ($\dot{M} \approx 10^{-3}\, M_\odot\ {\rm yr}^{-1}$ for $v_w = 1000\ {\rm km\ s}^{-1}$).
9. We compile the CSM densities of all radio-bright FBOTs from the literature and note that the environmental densities are strikingly similar, with $n \approx 10^6\ {\rm cm}^{-3}$ at $R \approx 10^{16}$ cm and an approximate profile of $\rho_{\rm CSM}(r) \propto r^{-3}$ over $R \approx 10^{16}$–10^{18} cm (Figure 10). This indicates that similar evolutionary processes and mass-loss mechanisms of the progenitor system are setting up these environments.
10. Our extensive X-ray and radio monitoring of AT 2024wpp and combined inferences from these observations favor a progenitor model that involves super-Eddington accretion onto a compact object capable of producing disk wind outflows with velocities up to $\sim 0.4c$.

LFBOTs remain one of the least understood classes of transients, with detailed multiwavelength data available only for a handful of events. Future wide-field time-domain surveys and rapid-response follow-up capabilities will be key to expanding this sample. Upcoming missions such as UVEX (S. R. Kulkarni et al. 2021) and ULTRASAT (Y. Shvartzvald et al. 2024) will enable the prompt discovery and early characterization of many more FBOTs. Coupled with coordinated multiwavelength campaigns, this will allow us to systematically probe the diversity of FBOT progenitors, their environments, and central engines.

Acknowledgments

We thank the anonymous referee for feedback. This Letter makes use of the following ALMA data: ADS/JAO.ALMA#2024.A.00003.T and ADS/JAO.ALMA#2024.A.00009.T. ALMA is a partnership of ESO (representing its member states), NSF (USA) and NINS (Japan), together with NRC (Canada), MOST and ASIAA (Taiwan), and KASI (Republic of Korea), in cooperation with the Republic of Chile. The Joint ALMA Observatory is operated by ESO, AUI/NRAO and NAOJ. The Allen Telescope Array refurbishment program and its ongoing operations are being substantially funded through the Franklin Antonio Bequest. Additional contributions from Frank Levinson, Greg Papadopoulos, the Breakthrough Listen Initiative, and other private donors have been instrumental in the renewal of the ATA. Breakthrough Listen is managed by the Breakthrough Initiatives, sponsored by the Breakthrough Prize Foundation. The Paul G. Allen Family Foundation provided major support for the design and construction of the ATA, alongside contributions from Nathan Myhrvold, Xilinx Corporation, Sun Microsystems, and other private donors. The ATA has also been supported by contributions from the US Naval Observatory and the US National Science Foundation. We thank the GMRT staff for making these observations possible. The GMRT is run by the National Centre for Radio Astrophysics of the Tata Institute of Fundamental Research. This research has made use of the NuSTAR Data Analysis Software (NuSTARDAS) jointly developed by the ASI Space Science Data Center (SSDC, Italy) and the California Institute of Technology (Caltech, USA). This research has made use of data obtained from the Chandra Data Archive provided by the Chandra X-ray Center (CXC). This Letter employs a list of Chandra data sets, obtained by the Chandra X-ray Observatory, contained in the Chandra Data Collection doi:10.25574/cdc.463. This research has made use of the XRT Data Analysis Software (XRTDAS) developed under the responsibility of the ASI Science Data Center (ASDC), Italy. This work made use of data supplied by the UK Swift Science Data Centre at the University of Leicester. This research has made use of data and software provided by the High Energy Astrophysics Science Archive Research Center (HEASARC), which is a service of the Astrophysics Science Division at NASA/GSFC.

R.M. acknowledges support by the National Science Foundation under award No. AST-2224255 and by NASA under grants 80NSSC22K1587, 80NSSC25K7591, and 80NSSC22K0898. G.M. acknowledges financial support from the INAF mini-grant "The high-energy view of jets and transient" (Bando Ricerca Fondamentale INAF 2022). B.D.M. acknowledges support from NASA AAG (grant No. 80NSSC22K0807), the Fermi Guest Investigator Program (grant No. 80NSSC24K0408), and the Simons Foundation (grant No. 727700). The Flatiron Institute is supported by the Simons Foundation. D.T. is supported by the Sherman Fairchild Postdoctoral Fellowship at Caltech. F.D.C. acknowledges support from the DGAPA/PAPIIT grant IN113424. D. L.C. acknowledges support from the Science and Technology Facilities Council (STFC) grant ST/X001121/1. N.L. thanks the LSST-DA Data Science Fellowship Program, which is funded by LSST-DA, the Brinson Foundation, the WoodNext Foundation, and the Research Corporation for Science Advancement Foundation; her participation in the program has benefited this work. C.T.C. and K.D.A. gratefully acknowledge support from NSF under grant AST-2307668 and from the Alfred P. Sloan Foundation.

Facilities: Swift (XRT and UVOT), AAVSO, CTIO:1.3m, CTIO:1.5m, CXO.

Software: astropy (Astropy Collaboration et al. 2013, 2018, 2022).

Appendix

Tables 3, 4, 5, 6, and 7 show radio observation logs and flux measurements of AT 2024wpp with ALMA, ATCA, ATA, MeerKAT, and GMRT, respectively. Table 8 shows the details of X-ray observations of AT 2024wpp with XMM, CXO, and NuSTAR.

Table 3
ALMA Observations of AT 2024wpp

Start Date (dd/mm/yyyy)	Project ID	Centroid MJD	Phase[a] (days)	Frequency (GHz)	Flux Density[b] (mJy)
14/10/2024	2024.A.00003.T	60597.22	18.92	97.5	0.076 ± 0.019
14/10/2024	2024.A.00003.T	60597.19	18.89	203.0	0.100 ± 0.024
31/10/2024	2024.A.00009.T	60614.06	35.76	97.5	1.282 ± 0.015
31/10/2024	2024.A.00009.T	60614.09	35.79	203.0	0.588 ± 0.031

Notes.
[a] With respect to first light.
[b] The uncertainties on flux measurements are 1σ.

Table 4
ATCA Observations of AT 2024wpp

Start Date (dd/mm/yyyy)	Project ID	Centroid MJD	Phase[a] (days)	Frequency (GHz)	Bandwidth (GHz)	Flux Density[b] (μJy)
10/10/2024	C3419	60593.00	14.70	16.7	2.0	<108
10/10/2024	C3419	60593.00	14.70	21.2	2.0	<108
10/10/2024	C3419	60593.00	14.70	43.0	2.0	<216
10/10/2024	C3419	60593.00	14.70	45.0	2.0	<216
14/10/2024	C3419	60597.48	19.18	16.7	2.0	<132
14/10/2024	C3419	60597.48	19.18	21.2	2.0	<132
30/10/2024	C3419	60613.47	35.17	5.5	2.0	178 ± 28
30/10/2024	C3419	60613.47	35.17	9.0	2.0	314 ± 20
30/10/2024	C3419	60613.47	35.17	16.7	2.0	442 ± 28
30/10/2024	C3419	60613.47	35.17	21.2	2.0	538 ± 53
14/11/2024	C3419	60628.37	50.07	5.5	2.0	224 ± 20
14/11/2024	C3419	60628.37	50.07	9.0	2.0	477 ± 18
14/11/2024	C3419	60628.37	50.07	16.7	2.0	734 ± 23
14/11/2024	C3419	60628.37	50.07	21.2	2.0	767 ± 76
14/11/2024	C3419	60628.37	50.07	34.0	2.0	611 ± 87
13/12/2024	C3419	60657.27	78.97	5.5	2.0	599 ± 82
13/12/2024	C3419	60657.27	78.97	9.0	2.0	847 ± 30
13/12/2024	C3419	60657.27	78.97	16.7	2.0	382 ± 42
13/12/2024	C3419	60657.27	78.97	21.2	2.0	274 ± 88
13/12/2024	C3419	60657.27	78.97	33.0	2.0	<300
13/12/2024	C3419	60657.27	78.97	35.0	2.0	<360
31/01/2025	C3419	60706.13	127.83	5.5	2.0	314 ± 35
31/01/2025	C3419	60706.13	127.83	9.0	2.0	202 ± 25
17/02/2025	C3419	60723.13	144.83	5.5	2.0	252 ± 25
17/02/2025	C3419	60723.13	144.83	9.0	2.0	337 ± 38
19/03/2025	C3419	60753.04	174.74	5.5	2.0	127 ± 19
19/03/2025	C3419	60753.04	174.74	9.0	2.0	143 ± 28

Notes.
[a] With respect to first light in observer frame.
[b] The uncertainties on flux measurements include map rms values (1σ) and a 5% systematic uncertainty on the flux density added in quadrature. The flux density upper limits are 3σ.

Table 5
ATA Observations of AT 2024wpp

Start Date (dd/mm/yyyy)	Project ID	Centroid MJD	Phase[a] (days)	Frequency (GHz)	Bandwidth (GHz)	Flux Density[b] (μJy)
09/10/2024	P053	60592.27	13.97	3.0	0.67	<570
09/10/2024	P053	60592.27	13.97	8.0	0.67	<1100
01/11/2024	P053	60615.21	36.91	3.0	0.67	<810
01/11/2024	P053	60615.21	36.91	8.0	0.67	<1440

Notes.
[a] With respect to first light.
[b] The flux density upper limits are 3σ.

Table 6
MeerKAT Observations of AT 2024wpp

Start Date (dd/mm/yyyy)	Project ID	Centroid MJD	Phase[a] (days)	Frequency (GHz)	Bandwidth (GHz)	Flux Density[b] (μJy)
31/10/2024	SCI-20230907-NA-01	60614.72	36.42	1.28	0.86	<66
15/11/2024	SCI-20230907-NA-01	60629.68	51.38	1.28	0.86	<60
11/12/2024	SCI-20230907-NA-01	60655.69	77.39	1.28	0.86	<75

Notes.
[a] With respect to first light.
[b] The flux density upper limits are 3σ.

Table 7
GMRT Observations of AT 2024wpp

Start Date (dd/mm/yyyy)	Project ID	Centroid MJD	Phase[a] (days)	Frequency (GHz)	Bandwidth (GHz)	Flux Density[b] (μJy)
01/11/2024	47_059	60615.00	36.70	1.25	0.40	<90
02/11/2024	47_059	60616.00	37.70	0.65	0.20	<86
02/11/2024	47_059	60616.00	37.70	0.44	0.20	<210
15/11/2024	47_059	60629.00	50.70	0.65	0.20	<81
02/12/2024	47_059	60646.00	67.70	0.44	0.20	<240
04/12/2024	47_059	60648.00	69.70	0.65	0.20	<75
26/01/2025	DDTC414	60701.55	123.25	1.25	0.40	<84

Notes.
[a] With respect to first light.
[b] The flux density upper limits are 3σ.

Table 8
X-Ray Observations of AT 2024wpp with NuSTAR, CXO, and XMM (PI: Margutti)

Instrument	Start Date (yyyy/mm/dd)	Mid-time[a] (days)	Obs ID	Exposure Time[b] (ks)
NuSTAR	2024-09-30	6.0	91001341002	41.5/41.0
NuSTAR	2024-10-06	11.0	91001341004	42.7/42.3
NuSTAR	2024-10-12	18.0	91001341006	57.1/56.6
NuSTAR	2024-11-16	52.3	80802406002	43.0/42.6
NuSTAR	2024-12-09	76.1	80802406004	35.7/37.1
CXO/ACIS-S	2024-10-13	19.9	30566	19.8
CXO/ACIS-S	2024-10-21	25.9	30567	19.8
CXO/ACIS-S	2024-11-14	49.7	30568	36.1
CXO/ACIS-S	2024-12-09	75.2	30642	36.2
XMM/EPIC-pn	2025-01-02	99.2	0903320501	33.1
XMM/EPIC-MOS1	2025-01-02	99.2	0903320501	44.8
XMM/EPIC-MOS2	2025-01-02	99.2	0903320501	44.8
XMM/EPIC-pn	2025-02-11	140.0	0903320601	13.3
XMM/EPIC-MOS1	2025-02-11	140.0	0903320601	40.4
XMM/EPIC-MOS2	2025-02-11	140.0	0903320601	40.4
XMM/EPIC-pn	2025-07-01	279.4	0903320701	42.7
XMM/EPIC-MOS1	2025-07-01	279.4	0903320701	44.8
XMM/EPIC-MOS2	2025-07-01	279.4	0903320701	44.8
XMM/EPIC-pn	2025-08-16	325.2	0903320801	26.8
XMM/EPIC-MOS1	2025-08-16	325.2	0903320801	40.1
XMM/EPIC-MOS2	2025-08-16	325.2	0903320801	40.1

Notes.
[a] With respect to first light.
[b] For NuSTAR we report the exposures for the A and B modules, respectively, after removing the interval of times severely affected by solar flares.

ORCID iDs

Nayana A.J. https://orcid.org/0000-0002-8070-5400
Raffaella Margutti https://orcid.org/0000-0003-4768-7586
Eli Wiston https://orcid.org/0009-0002-4843-2913
Tanmoy Laskar https://orcid.org/0000-0003-1792-2338
Giulia Migliori https://orcid.org/0000-0003-0216-8053
Ryan Chornock https://orcid.org/0000-0002-7706-5668
Timothy J. Galvin https://orcid.org/0000-0002-2801-766X
Natalie LeBaron https://orcid.org/0000-0002-2249-0595
Aprajita Hajela https://orcid.org/0000-0003-2349-101X
Collin T. Christy https://orcid.org/0000-0003-0528-202X
Itai Sfaradi https://orcid.org/0000-0003-0466-3779
Daichi Tsuna https://orcid.org/0000-0002-6347-3089
Olivia Aspegren https://orcid.org/0000-0001-5674-8403
Fabio De Colle https://orcid.org/0000-0002-3137-4633
Brian D. Metzger https://orcid.org/0000-0002-4670-7509
Wenbin Lu https://orcid.org/0000-0002-1568-7461
Paz Beniamini https://orcid.org/0000-0001-7833-1043
Daniel Kasen https://orcid.org/0000-0002-5981-1022
Edo Berger https://orcid.org/0000-0002-9392-9681
Brian W. Grefenstette https://orcid.org/0000-0002-1984-2932
Kate D. Alexander https://orcid.org/0000-0002-8297-2473
G. C. Anupama https://orcid.org/0000-0003-3533-7183
Deanne L. Coppejans https://orcid.org/0000-0001-5126-6237
Luigi F. Cruz https://orcid.org/0000-0001-5576-2254
David R DeBoer https://orcid.org/0000-0003-3197-2294
Maria R. Drout https://orcid.org/0000-0001-7081-0082
Wael Farah https://orcid.org/0000-0002-0161-7243
Xiaoshan Huang https://orcid.org/0000-0003-2868-489X
W. V. Jacobson-Galán https://orcid.org/0000-0003-1103-3409
Dan Milisavljevic https://orcid.org/0000-0002-0763-3885
Alexander W. Pollak https://orcid.org/0000-0002-3430-7671
Nathan J. Roth https://orcid.org/0000-0002-6485-2259
Huei Sears https://orcid.org/0000-0001-8023-4912
Andrew Siemion https://orcid.org/0000-0003-2828-7720
Sofia Z. Sheikh https://orcid.org/0000-0001-7057-4999
James F. Steiner https://orcid.org/0000-0002-5872-6061
Indrek Vurm https://orcid.org/0000-0003-1336-4746

References

Andreoni, I., Coughlin, M. W., Perley, D. A., et al. 2022, Natur, 612, 430
Antoni, A., & Quataert, E. 2022, MNRAS, 511, 176
Arcavi, I., Wolf, W. M., Howell, D. A., et al. 2016, ApJ, 819, 35
Astropy Collaboration, Price-Whelan, A. M., Lim, P. L., et al. 2022, ApJ, 935, 167
Astropy Collaboration, Price-Whelan, A. M., Sipőcz, B. M., et al. 2018, AJ, 156, 123
Astropy Collaboration, Robitaille, T. P., Tollerud, E. J., et al. 2013, A&A, 558, A33
Bell, A. R. 1978, MNRAS, 182, 147
Beniamini, P., Piran, T., & Matsumoto, T. 2023, MNRAS, 524, 1386
Berger, E., Zauderer, A., Pooley, G. G., et al. 2012, ApJ, 748, 36
Björnsson, C. I. 2024, ApJ, 963, 93
Björnsson, C. I., & Keshavarzi, S. T. 2017, ApJ, 841, 12
Blandford, R., & Eichler, D. 1987, PhR, 154, 1
Blandford, R. D., & Begelman, M. C. 1999, MNRAS, 303, L1
Blandford, R. D., & Ostriker, J. P. 1978, ApJL, 221, L29
Bright, J. S., Margutti, R., Matthews, D., et al. 2022, ApJ, 926, 112
Bright, J. S., Rhodes, L., Farah, W., et al. 2023, NatAs, 7, 986
Burrows, D. N., Hill, J. E., Nousek, J. A., et al. 2005, SSRv, 120, 165
Caprioli, D. 2015, ICRC, 34, 8
CASA Team, Bean, B., Bhatnagar, S., et al. 2022, PASP, 134, 114501
Cash, W. 1979, ApJ, 228, 939
Cendes, Y., Alexander, K. D., Berger, E., et al. 2021, ApJ, 919, 127
Chevalier, R. A. 1998, ApJ, 499, 810
Chevalier, R. A., Fransson, C., & Nymark, T. K. 2006, ApJ, 641, 1029
Chrimes, A. A., Coppejans, D. L., Jonker, P. G., et al. 2024a, A&A, 691, A329
Chrimes, A. A., Jonker, P. G., Levan, A. J., et al. 2024b, MNRAS, 527, L47
Coppejans, D. L., Margutti, R., Terreran, G., et al. 2020, ApJL, 895, L23
Dessart, L., Hillier, D. J., Sukhbold, T., Woosley, S. E., & Janka, H. T. 2021, A&A, 656, A61
Dessart, L., Yoon, S.-C., Aguilera-Dena, D. R., & Langer, N. 2020, A&A, 642, A106
Drout, M. R., Chornock, R., Soderberg, A. M., et al. 2014, ApJ, 794, 23
Dwarkadas, V. V. 2025, Univ, 11, 161
Eftekhari, T., Berger, E., Metzger, B. D., et al. 2022, ApJ, 935, 16
Ercolino, A., Jin, H., Langer, N., & Dessart, L. 2025, A&A, 696, A103
Evans, P. A., Beardmore, A. P., Page, K. L., et al. 2009, MNRAS, 397, 1177
Fox, O. D., & Smith, N. 2019, MNRAS, 488, 3772
Gehrels, N., Chincarini, G., Giommi, P., et al. 2004, ApJ, 611, 1005
Gompertz, B. P., Fruchter, A. S., & Pe'er, A. 2018, ApJ, 866, 162
Gottlieb, O., Tchekhovskoy, A., & Margutti, R. 2022, MNRAS, 513, 3810
Greisen, E. W. 2003, in Information Handling in Astronomy—Historical Vistas, ed. A. Heck (Dordrecht: Kluwer), 109
Gutiérrez, C. P., Mattila, S., Lundqvist, P., et al. 2024, ApJ, 977, 162
HI4PI Collaboration, Ben Bekhti, N., Flöer, L., et al. 2016, A&A, 594, A116
Ho, A. Y. Q., Bremer, M., Schulze, S., & Perley, D. 2023a, TNSAN, 100, 1
Ho, A. Y. Q., Margalit, B., Bremer, M., et al. 2022, ApJ, 932, 116
Ho, A. Y. Q., Perley, D. A., Chen, P., et al. 2023b, Natur, 623, 927
Ho, A. Y. Q., Perley, D. A., Gal-Yam, A., et al. 2023c, ApJ, 949, 120
Ho, A. Y. Q., Perley, D. A., Kulkarni, S. R., et al. 2020, ApJ, 895, 49
Ho, A. Y. Q., Phinney, E. S., Ravi, V., et al. 2019, ApJ, 871, 73
Ho, A. Y. Q., Srinivasaragavan, G., Perley, D., et al. 2024, TNSAN, 272, 1
Hollenbach, D., Johnstone, D., Lizano, S., & Shu, F. 1994, ApJ, 428, 654
Horesh, A., Stockdale, C., Fox, D. B., et al. 2013, MNRAS, 436, 1258
Kashi, A., & Soker, N. 2011, MNRAS, 417, 1466
Keto, E. 2007, ApJ, 666, 976
Khatami, D. K., & Kasen, D. N. 2024, ApJ, 972, 140
King, A., Lasota, J.-P., & Middleton, M. 2023, NewAR, 96, 101672
Kitaki, T., Mineshige, S., Ohsuga, K., & Kawashima, T. 2021, PASJ, 73, 450
Kremer, K., Lu, W., Piro, A. L., et al. 2021, ApJ, 911, 104
Kuin, N. P. M., Wu, K., Oates, S., et al. 2019, MNRAS, 487, 2505
Kulkarni, S. R., Harrison, F. A., Grefenstette, B. W., et al. 2021, arXiv:2111.15608
Leung, S.-C., Blinnikov, S., Nomoto, K., et al. 2020, ApJ, 903, 66
Leung, S.-C., Fuller, J., & Nomoto, K. 2021, ApJ, 915, 80
Li, W., Chornock, R., Leaman, J., et al. 2011, MNRAS, 412, 1473
MacLeod, M., & Loeb, A. 2020, ApJ, 895, 29
MacLeod, M., Macias, P., Ramirez-Ruiz, E., et al. 2017, ApJ, 835, 282
Margalit, B., & Metzger, B. D. 2016, MNRAS, 461, 1154
Margalit, B., & Quataert, E. 2021, ApJL, 923, L14
Margutti, R., AJ, N., Chornock, R., et al. 2024, TNSAN, 278, 1
Margutti, R., Metzger, B. D., Chornock, R., et al. 2019, ApJ, 872, 18
Margutti, R., Zaninoni, E., Bernardini, M. G., et al. 2013, MNRAS, 428, 729
Matsumoto, T., & Metzger, B. D. 2022, ApJ, 938, 5
Matsumoto, T., & Piran, T. 2023, MNRAS, 522, 4565
Matthews, D., Margutti, R., Metzger, B. D., et al. 2023, RNAAS, 7, 126
Matzner, C. D., & McKee, C. F. 1999, ApJ, 510, 379
Metzger, B. D. 2022, ApJ, 932, 84
Metzger, B. D., & Piro, A. L. 2014, MNRAS, 439, 3916
Metzger, B. D., Vurm, I., Hascoët, R., & Beloborodov, A. M. 2014, MNRAS, 437, 703
Migliori, G., Margutti, R., Metzger, B. D., et al. 2024, ApJL, 963, L24
Narayan, R., & Yi, I. 1995, ApJ, 444, 231
Nayana, A. J., & Chandra, P. 2021, ApJL, 912, L9
Nayana, A. J., Margutti, R., Laskar, T., et al. 2025, TNSAN, 114, 1
Ofek, E. O., Ozer, L., Konno, R., et al. 2025, arXiv:2508.18359
Offringa, A. R., & Smirnov, O. 2017, MNRAS, 471, 301
Ohsuga, K. 2007, PASJ, 59, 1033
Pejcha, O., Metzger, B. D., & Tomida, K. 2016a, MNRAS, 455, 4351
Pejcha, O., Metzger, B. D., & Tomida, K. 2016b, MNRAS, 461, 2527
Pejcha, O., Metzger, B. D., Tyles, J. G., & Tomida, K. 2017, ApJ, 850, 59
Pellegrino, C., Howell, D. A., Vinkó, J., et al. 2022, ApJ, 926, 125
Perley, D. A., Ho, A. Y. Q., Petitpas, G., & Keating, G. 2022, GCN, 31627, 1
Perley, D. A., Mazzali, P. A., Yan, L., et al. 2019, MNRAS, 484, 1031
Perley, D. A., Qin, Y., Rich, R. M., et al. 2024, TNSAN, 280, 1
Planck Collaboration, Aghanim, N., Akrami, Y., et al. 2020, A&A, 641, A6
Pursiainen, M., Childress, M., Smith, M., et al. 2018, MNRAS, 481, 894

Pursiainen, M., Killestein, T. L., Kuncarayakti, H., et al. 2025, MNRAS, 537, 3298
Quataert, E., Lecoanet, D., & Coughlin, E. R. 2019, MNRAS, 485, L83
Renzo, M., Farmer, R., Justham, S., et al. 2020, A&A, 640, A56
Rest, A., Garnavich, P. M., Khatami, D., et al. 2018, NatAs, 2, 307
Rybicki, G. B., & Lightman, A. P. 1979, Radiative Processes in Astrophysics (New York: Wiley)
Sadowski, A., & Narayan, R. 2015, MNRAS, 453, 3213
Sadowski, A., & Narayan, R. 2016, MNRAS, 456, 3929
Sari, R., Piran, T., & Halpern, J. P. 1999, ApJL, 519, L17
Schroeder, G., Ho, A. Y. Q., & Perley, D. A. 2024, TNSAN, 314, 1
Sfaradi, I., Margutti, R., Chornock, R., et al. 2025, arXiv:2508.03807
Sfaradi, I., Margutti, R., Farah, W., et al. 2024, TNSAN, 290, 1
Shvartzvald, Y., Waxman, E., Gal-Yam, A., et al. 2024, ApJ, 964, 74
Sironi, L., & Spitkovsky, A. 2009, ApJ, 698, 1523
Sironi, L., & Spitkovsky, A. 2011, ApJ, 726, 75
Smith, N. 2014, ARA&A, 52, 487
Spitkovsky, A. 2008, ApJL, 682, L5
Srinivasaragavan, G., Ho, A., Perley, D., et al. 2024, TNSAN, 276, 1
Takahashi, H. R., & Ohsuga, K. 2017, ApJL, 845, L9
Tampo, Y., Tanaka, M., Maeda, K., et al. 2020, ApJ, 894, 27
Tan, J. C., Matzner, C. D., & McKee, C. F. 2001, ApJ, 551, 946
Tanaka, M., Tominaga, N., Morokuma, T., et al. 2016, ApJ, 819, 5
Tauris, T. M., Langer, N., & Podsiadlowski, P. 2015, MNRAS, 451, 2123
Titarchuk, L., & Seifina, E. 2021, MNRAS, 501, 5659
Tsuna, D., & Lu, W. 2025, ApJ, 986, 84
Vurm, I., & Metzger, B. D. 2021, ApJ, 917, 77
Waxman, E., & Shvarts, D. 1993, PhFlA, 5, 1035
Weiler, K. W., Panagia, N., Montes, M. J., & Sramek, R. A. 2002, ARA&A, 40, 387
Weiler, K. W., Williams, C. L., Panagia, N., et al. 2007, ApJ, 671, 1959
Woosley, S. E. 2017, ApJ, 836, 244
Wu, S. C., & Fuller, J. 2022, ApJL, 940, L27
Yao, Y., Ho, A. Y. Q., Medvedev, P., et al. 2022, ApJ, 934, 104
Yoshioka, S., Mineshige, S., Ohsuga, K., Kawashima, T., & Kitaki, T. 2024, PASJ, 76, 1015
Yuan, Q., Wang, Q. D., Lei, W.-H., Gao, H., & Zhang, B. 2016, MNRAS, 461, 3375